Zhu et al. *Zool. Res.* 2025, 46(2): 429−445
https://doi.org/10.24272/j.issn.2095-8137.2024.399
https://cstr.cn/32248.14.zr.2024.399

ZR | Zoological Research

Article Open Access

Single-cell sequencing analysis reveals the essential role of the m^{6}A reader YTHDF1 in retinal visual function by regulating TULP1 and DHX38 translation

Xian-Jun Zhu[1,2,3,4,#,*], Xiao-Yan Jiang[2,#], Wen-Jing Liu[2,#], Yu-Di Fan[2], Guo Liu[2,3], Shun Yao[1,5], Kuan-Xiang Sun[2], Jun-Yao Chen[2], Bo Lei[1,5,*], Ye-Ming Yang[2,4,*]

[1] *Henan Branch of National Clinical Research Center for Ocular Diseases*, *Henan Eye Hospital*, *People's Hospital of Zhengzhou University*, *Henan Provincial People's Hospital*, *Zhengzhou*, *Henan* 450003, *China*

[2] *Sichuan Provincial Key Laboratory for Human Disease Gene Study*, *Center for Medical Genetics*, *Sichuan Provincial People's Hospital*, *University of Electronic Science and Technology of China*, *Chengdu*, *Sichuan* 610072, *China*

[3] *Sichuan-Chongqing Joint Key Laboratory for Pathology and Laboratory Medicine*, *Jinfeng Laboratory*, *Chongqing* 400039, *China*

[4] *Qinghai Key Laboratory of Qinghai Tibet Plateau Biological Resources*, *Chinese Academy of Sciences and Qinghai Provincial Key Laboratory of Tibetan Medicine Research*, *Northwest Institute of Plateau Biology*, *Xining*, *Qinghai* 810008, *China*

[5] *Eye Institute*, *Henan Academy of Innovations in Medical Science*, *Zhengzhou*, *Henan* 451162, *China*

ABSTRACT

N6-methyladenosine (m^{6}A) modification of mRNA is a critical post-transcriptional regulatory mechanism that modulates mRNA metabolism and neuronal function. The m^{6}A reader YTHDF1 has been shown to enhance the translational efficiency of m^{6}A-modified mRNAs in the brain and is essential for learning and memory. However, its role in the mature retina remains unclear. Herein, we report a novel role of *Ythdf1* in the maintenance of retinal function using a genetic knockout model. Loss of *Ythdf1* resulted in impaired scotopic electroretinogram (ERG) responses and progressive retinal degeneration. Detailed analyses of rod photoreceptors confirmed substantial degenerative changes in the absence of ciliary defects. Single-cell RNA sequencing revealed comprehensive molecular alterations across all retinal cell types in *Ythdf1*-deficient retinas. Integrative analysis of methylated RNA immunoprecipitation (MeRIP) sequencing and RIP sequencing identified *Tulp1* and *Dhx38*, two inheritable retinal degeneration disease-associated gene homologs, as direct targets of YTHDF1 in the retina. Specifically, YTHDF1 recognized and bound m^{6}A-modified *Tulp1* and *Dhx38* mRNA at the coding sequence (CDS), enhancing their translational efficiency without altering mRNA levels. Collectively, these findings highlight the essential role of YTHDF1 in preserving visual function and reveal a novel regulatory mechanism of m^{6}A reader proteins in retinal degeneration, identifying potential therapeutic targets for severe retinopathies.

Keywords: Epitranscriptomics; N6-methyladenosine (m^{6}A); Inherited retinal dystrophies (IRDs); YTHDF1; Single-cell RNA sequencing; Photoreceptor degeneration

INTRODUCTION

N6-methyladenosine (m^{6}A) is the most prevalent post-transcriptional modification of eukaryotic messenger RNA (mRNA) and non-coding RNAs, including transfer RNA (tRNA), ribosomal RNA (rRNA), microRNA, and long non-coding RNA. It plays an essential role in the regulation of RNA metabolism, influencing processes such as splicing, stability, translation, and nuclear export (Barbieri et al., 2017; Huang et al., 2018; Shi et al., 2020; Wang et al., 2014). m^{6}A modification is a dynamic and reversible process tightly regulated by multiple factors including methyltransferases, demethylases, and m^{6}A-recognizing proteins. For instance, m^{6}A is installed by the m^{6}A methyltransferase complex ("writer"), which consists of core subunits METTL3, METTL14, and Wilm's-tumor-1-associated protein (WTAP), as well as several accessory cofactors such as RNA-binding motif protein 15 (RBM15)/15B, VIRMA, and HAKAI (Bawankar et al., 2021; Liu et al., 2014; Ping et al., 2014; Wang et al., 2021; Yue et al., 2018). This modification can be removed by demethylases ("eraser"), including ALKB homolog 5 (ALKBH5)

Received: 11 November 2024; Accepted: 15 January 2025; Online: 16 January 2025

Foundation items: This study was supported by the National Natural Science Foundation of China (82371083, 82471100, 82121003, 82271084), Program of Science and Technology International Cooperation Project of Qinghai province (China) (2022-HZ-814)

[#]Authors contributed equally to this work

*Corresponding authors, E-mail: xjzhu@uestc.edu.cn; bolei99@126.com; nickyym@uestc.edu.cn

and fat mass and obesity-associated protein (FTO) (Jia et al., 2011; Liu et al., 2014; Zheng et al., 2013). Recognition of m^{6}A-modified transcripts is mediated by a diverse set of RNA-binding proteins ("readers"), which bind to the m^{6}A motif and regulate RNA metabolism, including YTH N6-methyladenosine RNA binding protein 1–3 (YTHDF1–3) (Liu et al., 2020b), YTH domain containing 1, 2 (YTHDC1, 2) (Ma et al., 2021), insulin-like growth factor 2 mRNA binding proteins (IGF2BP1–3) (Huang et al., 2018), and eukaryotic translation initiation factor 3 (eIF3) (Meyer et al., 2015). Moreover, RNA-binding protein proline-rich coiled-coil 2A(PPRC2) has been identified as an m^{6}A-interacting protein involved in oligodendrocyte myelination (Wu et al., 2019). Mounting evidence suggests that m^{6}A methylation and its binding proteins play critical roles in various biological processes, including embryonic development, cellular differentiation, innate immune responses, and cancer (Winkler et al., 2019; Yang et al., 2022a, 2023). In the retina, METTL14 is essential for retinal photoreceptor survival by regulating phototransduction and ciliogenesis (Yang et al., 2022b). Similarly, *Mettl14* is indispensable for both cortical and retinal neurogenesis (Niu et al., 2022a), and conditional deletion of *Mettl3* using Six3-Cre in retinal progenitor cells has shown that METTL3 is essential for late-stage retinogenesis (Xin et al., 2022). More recently, ALKBH5 has been implicated in age-related macular degeneration (AMD), with its overexpression leading to retinal pigment epithelium (RPE) dysfunction and choroidal neovascularization (CNV) (Sun et al., 2023). Collectively, these findings highlight the fundamental role of m^{6}A modification in retinal development and homeostasis.

The m^{6}A reader YTHDF1 has been shown to enhance the translational efficiency of m^{6}A-modified mRNAs (Liu et al., 2020a). In the brain, *Ythdf1* is highly expressed in the hippocampus, where it facilitates protein synthesis in response to stimulation, with *Ythdf1* deletion in mice resulting in learning and memory defects (Shi et al., 2018). However, subsequent studies have suggested that YTHDF1 is not required for memory formation, with YTHDF2 playing a more prominent role in this process (Zhuang et al., 2023). In the brain, both YTHDF1 and YTHDF2 contribute to cortical neurogenesis, while in the retina, YTHDF1, YTHDF2, and YTHDF3 function collaboratively in retinal neurogenesis, suggesting functional redundancy of different YTHDFs (Niu et al., 2022a). Conditional knockout (KO) of *Ythdf2* in retinal ganglion cells (RGCs) increases dendritic branching and improves visual acuity (Niu et al., 2022b). These results suggest that different YTHDF proteins exhibit functional overlap in neuronal development but assume specific roles in postmitotic neurons. YTHDF1 is also essential for commissural axon guidance in dorsal spinal commissural neurons, where it regulates translation of Robo3.1 mRNA (Zhuang et al., 2019). Conditional KO of *Ythdf1* or *Ythdf2* in cerebellar granule cells (GC) enhances axon growth and synapse formation between GC-Purkinje cells through translational regulation of *Dvl1* and *Wnt5a* (Yu et al., 2021). These findings underscore the tissue-specific and functionally distinct roles of YTHDF proteins in maintaining postmitotic neuronal integrity. However, the role of YTHDF1 in the maintenance of mature retinal neurons remains unknown.

This study investigated the function of YTHDF1 in visual processing and retinal neuron homeostasis by generating *Ythdf1* KO (*Ythdf1*$^{-/-}$) mice. Loss of *Ythdf1* resulted in reduced scotopic electroretinogram (ERG) responses and progressive retinal degeneration, recapitulating the retinal degeneration observed in *Mettl14*^{RKO} mice (Yang et al., 2022b). Single-cell transcriptomic profiling and RNA immunoprecipitation sequencing (RIP-seq) revealed that YTHDF1 regulated retinal function by enhancing the translation of *Tulp1* and *Dhx38*, a process largely dependent on its YTH domain. Moreover, YTHDF1 selectively recognized and interacted with m^{6}A-modified *Tulp1* and *Dhx38* at coding sequence (CDS) regions near the stop codon, promoting their translation in an m^{6}A-dependent manner. Collectively, these findings establish YTHDF1 as a key regulator of visual function and photoreceptor survival, identifying potential therapeutic targets for retinal degeneration.

MATERIALS AND METHODS

Mouse models

All animal experimental protocols were approved by the Institutional Animal Care and Use Committee of Sichuan Provincial People's Hospital (Chengdu, Sichuan, China) (Approval number: LS-20180063) and were conducted in accordance with the ARVO Statement for the Use of Animals in Ophthalmic and Vision Research. All mice were housed in a controlled environment under a temperature of 24±2°C and a 12 h light/dark cycle, with free access to food and water. Mice were maintained on a C57BL/6J background. Male and female animals were examined, with similar findings reported for both sexes.

Conventional *Ythdf1* KO mice were generated using the CRISPR/Cas9 system by Suzhou Cyagen Biosciences Inc. (Suzhou, China). Briefly, a single-guide RNA (sgRNA) targeting the third exon of the *Ythdf1* gene (5'-GTTCGG TCCCACCTTGGGGCGGG -3') was designed and synthesized. The KO allele was engineered to delete a 777 base pair region encompassing exon 3 and introduce a frameshift deletion (−80 bp) in the *Ythdf1* transcript, generating a premature termination codon after the 16th amino acid residue. Genotypes of KO alleles were confirmed by Sanger sequencing using specific primers (Supplementary Table S1). Mice carrying this allele were backcrossed with C57BL/6J mice for four generations to establish a genetically stable background. Subsequently, progeny mice were intercrossed to generate homozygous *Ythdf1* KO mice (*Ythdf1*$^{-/-}$) for further investigation. Wild-type (*Ythdf1*$^{+/+}$) littermates were used as controls. All mice were housed in ventilated, specific pathogen-free (SPF) cages under thermostatic conditions (24°C) with a 12 h light-dark cycle.

Genotyping

Genomic DNA was extracted from mouse tail biopsies and genotyped via polymerase chain reaction (PCR). The *Ythdf1* KO allele was genotyped using specific primers (Supplementary Table S1). PCR amplification was performed using a master mix (Invitrogen, USA) following the manufacturer's instructions. The thermal cycling protocol included an initial denaturation at 95°C for 5 min, followed by 32 cycles at 95°C for 15 s, 60°C for 30 s, and 72°C for 30 s. Amplification with the F1-R primer pair produced a 792 bp fragment in homozygous KO mice, while the F2-R primer pair generated a 483 bp product in wild-type mice. Heterozygous mice exhibited both amplicons. PCR products were resolved via electrophoresis on a 3% agarose gel.

Histological analysis

For histological evaluation, enucleated eyes from control and mutant mice were fixed overnight in a solution containing 1.22% glutaraldehyde and 0.8% paraformaldehyde (PFA) in 0.08 mol/L phosphate buffer. Samples were then embedded in paraffin and sectioned at a thickness of 5 μm. To ensure consistency in quantification, the globes were embedded in the same orientation, and sections containing the optic nerve (ON) were selected for hematoxylin and eosin (H&E) staining following standard protocols. The sections were scanned using a Pannoramic DESK slide scanner (3D HISTECH, Hungary) and analyzed using CaseViewer v.2.4 (3D HISTECH, Hungary). Outer nuclear layer (ONL) thickness was measured at 250 μm intervals from the ON. At least three sections per mouse, from three mice per genotype, were analyzed and averaged.

Electroretinography

For electroretinographic evaluation, mice underwent overnight dark adaptation before anesthesia was induced via intraperitoneal injection of xylazine (80 mg/kg) and ketamine (16 mg/kg) in normal saline. Pupillary dilation was achieved with a single drop of 0.5% tropicamide phenylephrine, and local anesthesia was administered using one drop of 0.5% oxybuprocaine hydrochloride. To preserve dark adaptation, all handing, preparation, and electrode placements were performed under dim red light. ERG recordings were acquired using a Roland electroretinogram recorder and Ganzfeld Q450 stimulator (Roland Consult, Germany). Scotopic (dark-adapted) ERG recordings were performed first, using a series of stimuli at increasing luminance levels (0.01, 0.03, 0.1, 3.0, and 10.0 cds/m^2). Scotopic oscillatory potentials were then recorded under 3.0 cds/m^2 light stimulation. Following a 10 min light adaptation period, photopic responses were assessed, including photopic 3.0 ERG and photopic 3.0 flicker responses under corresponding stimulation conditions.

Retinal dissociation and single-cell RNA sequencing (scRNA-seq)

For scRNA-seq, four retinas were collected per experimental group. Mice were euthanized with carbon dioxide, and their eyes were enucleated for retinal tissue isolation. Retinas were carefully dissected under a stereomicroscope, immediately placed in ice-cold phosphate-buffered saline (PBS), and finely minced on ice. Retinas from each genotype were pooled, rapidly frozen, and immediately transported to BD Biosciences (China) for further processing. For enzymatic dissociation, retinal tissue was transferred into a digestion solution containing either 0.125% trypsin-EDTA or a mixture of papain and DNase I, prepared according to the manufacturer's recommendations. Samples were incubated at 37°C for 10–15 min with gentle agitation for extracellular matrix dissociation. Following enzymatic digestion, the partially dissociated tissue was gently triturated using a fire-polished glass pipette or fine-bore pipette tips to generate a single-cell suspension. The suspension was filtered through a 40 μm cell strainer to remove cell aggregates and debris. The filtrate was then centrifuged at 300 ×*g* for 5 min at 4°C, and the pellet was resuspended in Hank's Balanced Salt Solution (HBSS) supplemented with 1% bovine serum albumin (BSA) to improve cell viability. Single-cell processing was conducted using the BD Rhapsody Single-Cell RNA Sequencing (scRNA-seq) platform (BD Biosciences, China) (Chen et al., 2021; Xia et al., 2023). Cells were labeled at room temperature for 20 min and washed via centrifugation at 500 ×*g* for 5 min at 4°C. Single-cell isolation in microwells, cell lysis, and capture of polyadenylated mRNAs using barcoded magnetic capture beads were performed according to the manufacturer's instructions. Magnetically retrieved beads were pooled into a single tube for reverse transcription, during which unique molecular identifiers (UMIs) were incorporated into cDNA molecules. Whole-transcriptome amplification and sample-tag sequencing libraries were generated using the BD Rhapsody single-cell whole-transcriptome amplification workflow. Library quantification was performed using a High Sensitivity DNA chip on the Bioanalyzer 2200 system (Agilent, USA), as well as a Qubit High Sensitivity DNA assay (Thermo Fisher Scientific, USA). Sequencing libraries were then subjected to paired-end 150 bp sequencing using the HiSeq X Ten platform (Illumina, USA).

Single-cell analysis

Raw count data were processed using Seurat single- cell analysis software (v.4.1.3; https://github.com/satijalab/seurat). Quality control was performed to remove low-quality cells and outliers, ensuring robust downstream analysis. Cells were retained for further processing if they expressed 200–10 000 genes, contained 364–31 000 UMIs, and expressed <10% mitochondrial genes. After filtering, a dataset consisting of 35 208 genes across 28 399 cell matrices was obtained for further analysis.

Cell type annotation was performed based on established retinal marker genes to identify different cell populations (Menon et al., 2019). Clustering was visualized using *t*-distributed stochastic neighbor embedding (*t*-SNE), with additional *t*-SNE projections generated to display individual samples and sample groups. Other visualizations, including bar plots, boxplots, violin plots, and heatmaps, were generated using customized R scripts with ggplot2 (v.3.4.3) and Complex Heatmap (v.2.14.0). Differential gene expression analysis was performed using the FindMarkers function in Seurat with the Wilcoxon rank-sum test. Differentially expressed genes (DEGs) were defined based on a fold change threshold of >1.5 or <1/1.5, with statistical significance set at $P<0.05$. Functional enrichment analysis of DEGs was performed using clusterProfiler R package (v.4.4.4) with default settings. Gene Ontology (GO) terms with an adjusted $P<0.05$ (calculated using the hypergeometric test and corrected using the Benjamini-Hochberg method) were considered significantly enriched. The top eight enriched GO terms, ranked by ascending unadjusted *P*-values, were selected for visualization.

Immunohistochemistry

For immunohistochemical analysis, eyes were collected from euthanized mice and fixed in 4% PFA prepared in 100 mmol/L phosphate buffer (pH 7.4) for 1h at 4°C. Following fixation, tissues were cryoprotected in 30% sucrose for 2 h. The lenses were removed, and the eyes were embedded in an optimal cutting temperature (OCT) compound, then cryosectioned at a thickness of 10 μm. Sections were blocked and permeabilized with 10% normal donkey serum and 0.2% Triton X-100 in phosphate buffer for 1 h. Primary antibodies (listed in Supplementary Table S2) were applied, and sections were incubated overnight at 4°C. After rinsing in PBS three times, sections were incubated with Alexa Fluor 594/488-conjugated goat anti-mouse/rabbit secondary antibodies (Cat# A11005 and A11008, Invitrogen, USA, 1:500 dilution). Nuclei were

counterstained with 4',6-diamidino-2-phenylindole (DAPI, Cat# D8417, Sigma, USA) for 1 h at room temperature. Images were captured on a Zeiss LSM 800 confocal scanning microscope (Germany), and fluorescence intensity was quantified using ZEN v.2.3 imaging software.

Retinal flat mounts and RGC count

Retinas were dissected from enucleated eyes, flattened, and immersed in 4% PFA for 24h at 4°C. After fixation, tissues were blocked in PBS containing 1% BSA and 0.5% Triton X-100 before incubation with a polyclonal rabbit anti-Brn3a antibody (Cat# ab245230, Abcam, USA, 1:200 dilution) for 12 h at 4 °C. After several washes, the retinas were incubated for 4 h at room temperature with Alexa Fluor 488-conjugated goat anti-rabbit secondary antibody (Cat# A11008, Invitrogen, USA, 1:250 dilution), and subsequently washed with PBS. To quantify RGC loss, each retina was divided into four quadrants—nasal, temporal, superior, and inferior—with RGC counts performed in four predefined zones within each quadrant, located 1 mm from the ON head (Nadal-Nicolás et al., 2023). Cell counts were performed independently by two investigators in a blinded fashion, and results were averaged to minimize bias.

Transmission electron microscopy (TEM)

For ultrastructural analysis, anesthetized mice underwent transcardial perfusion with PBS, followed by fixation with 2.5% glutaraldehyde in cacodylate buffer (pH 7.2). Enucleated eyes were postfixed overnight at 4°C in 2.5% glutaraldehyde in cacodylate buffer. Retinal sections were obtained at 100 mm intervals using a vibratome and subsequently incubated in 1% osmium tetroxide for 1 h. After washing in 0.1 mol/L phosphate buffer, tissues were dehydrated through a graded ethanol series followed by propylene oxide and embedded in Epon resin (25 g of Epon 812, 13 g of dodecenyl succinic anhydride, 12 g of methyl nadic anhydride, and 1 mL of 2,4,6-tris (dimethylaminomethyl) phenol (DMP-30), Electron Microscopy Sciences). Ultrathin sections (70 nm) were cut, stained with uranyl acetate and lead citrate, and imaged using a Philips CM120 scanning transmission electron microscope (the Netherlands).

Western blot analysis

Retinal tissues were lysed in radioimmunoprecipitation assay buffer containing a protease inhibitor cocktail (Cat# 11697498001, Roche, USA) and phosphatase inhibitor (Cat# 4906845001, Roche, USA). Protein concentrations were determined using a DC Protein Assay (Cat# 500-0122, Bio-Rad, USA) according to the manufacturer's instructions. Equal amounts of protein were separated via sodium dodecyl sulfate-polyacrylamide gel electrophoresis (SDS-PAGE) and transferred onto nitrocellulose (NC) membranes (Cat# HATF00010, Millipore, USA). The blots were blocked with 8% nonfat dry milk in Tris-buffered saline (TBS) with Tween® 20 detergent for 2 h at room temperature before overnight incubation at 4°C with primary antibodies (Supplementary Table S2) diluted in blocking solution. After washing, membranes were incubated with horseradish peroxidase (HRP)-conjugated anti-mouse or anti-rabbit secondary antibodies (1:5 000; Bio-Rad, USA), and signals were developed using a SuperSignal™ West Pico PLUS Chemiluminescent Substrate (Cat# 34577, Thermo, USA). Immunoreactive band intensities were quantified using ImageJ gel analysis tools, with protein levels normalized to GAPDH. All experiments were conducted using at least three independent biological samples, with each experiment repeated at least twice. Representative blots are presented.

RNA extraction and reverse transcription-quantitative PCR (RT-qPCR)

Total retinal RNA was extracted using TRIzol reagent (Cat# T9424, Sigma, USA) as recommended by the manufacturer. First-strand cDNA was synthesized using an iScript cDNA Synthesis Kit (Cat# 170-8890, Bio-Rad, USA). Quantitative PCR was performed as described previously (Hassan et al., 2023) using iTaq SYBRMix (Cat# 1725120, Bio-Rad, USA) and the CFX384 Touch Real-Time PCR Detection System (Cat# BJ005303, Bio-Rad, USA). Primers were designed using Primer3Plus or obtained from published resources (Supplementary Table S1). All target genes were normalized to actin mRNA levels, and relative fold changes were calculated using delta-delta Ct analysis.

RIP-seq

RIP-seq, including immunoprecipitation (IP), high-throughput sequencing, and data analysis, was conducted by Seqhealth Technology (China). Briefly, retinal tissue was collected, flash-frozen in liquid nitrogen, and homogenized using a tissue lyser. A portion of the lysate (20%) was reserved as "input", while the remaining 80% underwent IP using anti-YTHDF1 antibodies. RNA was extracted from both input and IP samples, and strand-specific RNA-seq libraries were constructed using a KC-Digital^{TM} Stranded mRNA Library Prep Kit for Illumina® (Cat# DR08502, Wuhan Seqhealth, China) following the manufacturer's instructions. Libraries containing fragments between 200–500 bp were enriched, quantified, and sequenced on the NovaSeq 6000 platform (Illumina, USA) using the paired-end 150 bp (PE150) model. The enrichment ratio of a transcript in IP relative to input was calculated. Sequence motifs were identified using Homer. YTHDF1-binding mRNAs were identified based on a fold-change threshold of >2, with a statistical significance cutoff of P<0.05.

Methylated RNA immunoprecipitation (MeRIP)-qPCR and RIP-qPCR

Total RNA was extracted using TRIzol reagent (Cat# Solarbio, China) and purified with an EasyPure RNA Purification Kit (Cat# ER701-01, TransGen, China). For MeRIP-qPCR, RNA was incubated with anti-m^{6}A antibodies and subjected to IP using Magna MeRIP m^{6}A Kit (Millipore, #17–10499, USA) in accordance with the manufacturer's protocols. Enrichment of m^{6}A-containing mRNA was detected by RT-RT-qPCR with specific primers. For RIP-qPCR, retinal lysates were incubated overnight at 4°C with magnetic beads conjugated with 5 μg of anti-YTHDF1 or IgG antibodies using a Magna RIP Kit (Millipore, #17–700, USA). After proteinase K digestion, the remaining RNA was purified using TRIzol reagent and measured by RT-qPCR. The primers used for MeRIP- and RIP-qPCR are listed in Supplementary Table S1.

Cell culture and transfection

HEK293T cells were purchased from the National Infrastructure of Cell Line Resource (China) and authenticated by short tandem repeat (STR) profiling. Cells were cultured in high-glucose Dulbecco's Modified Eagle Medium (DMEM) (Hyclone, USA) supplemented with 10% fetal bovine serum (Gibco, USA) and 100 U/mL penicillin/streptomycin (Invitrogen, USA) in an incubator at 37°C with 5% CO_2. For transfection, cells were seeded in culture plates (Corning,

USA) and transiently transfected with constructed plasmids using Lipofectamine 3000 (Invitrogen, USA) following the manufacturer's instructions. Cell lysates were harvested at 48 h post-transfection for analysis.

Plasmid construction and luciferase reporter assays

Full-length wild-type CDS regions of *Tulp1* (*pmiRGLO-Tulp1-CDS*) and *Dhx38* (*pmiRGLO-Dhx38-CDS*) were synthesized and inserted downstream of the firefly luciferase gene in the pmirGLO reporter vector. A wild-type YTHDF1 pcDNA 3.1-expressing plasmid was constructed by Youbio (China). For dual-luciferase reporter assays, HEK293T cells were co-transfected with *pmiRGLO-Tulp1-CDS* or *pmiRGLO-Dhx38-CDS* plasmids along with wild-type YTHDF1 pcDNA 3.1-expressing plasmid using Lipofectamine 3000. After 48 h of transfection, luciferase activity was measured using reporter lysis buffer (Catalog #E3971, Promega, USA) and luciferase assay reagent with the Dual-Glo Luciferase Assay system according to the manufacturer's instructions. Firefly luciferase (F-Luc) activity was normalized to *Renilla* luciferase (R-Luc) to evaluate reporter translation efficiency. The mRNA levels of F-Luc and R-Luc were quantified by RT-qPCR, and translational efficiency was defined as the quotient of reporter protein production (F-Luc/R-Luc) divided by mRNA abundance, as described previously (Wang et al., 2015).

Statistical analysis

Statistical analyses were conducted using GraphPad Prism v.6. Normality was assessed using the Shapiro-Wilk test. For normally distributed data, statistical significance was determined using Student's *t*-test or one-way/two-way analysis of variance (ANOVA). Nonparametric tests were applied when normality assumptions were not met. Multiple comparisons were performed using Tukey's, Dunnett's, or Sidak's *post hoc* tests. A *P*-value <0.05 was considered statistically significant.

RESULTS

Construction and validation of *Ythdf1* KO mice

The m^{6}A-binding protein YTHDF1 is broadly expressed in the mouse retina and functions cooperatively with YTHDF2 and YTHDF3 to regulate retinal neurogenesis, although its loss alone does not impede retinal development (Niu et al., 2022a). We previously demonstrated that METTL14-mediated m^{6}A modification is essential for maintaining retinal function and homeostasis in adulthood (Yang et al., 2022b). However, the role of m^{6}A readers in the mature neural retina remains poorly understood.

To investigate the potential function of YTHDF1 in the human retina, publicly available single-cell transcriptomic data from the Human Protein Atlas (HPA) database (https://www.proteinatlas.org) were analyzed to assess the expression levels of YTHDF1 in human retinal cells. These data revealed that YTHDF1 is ubiquitously expressed across the entire retina and different retinal cell types, with particularly high enrichment in rod photoreceptors and Müller glial cells (Supplementary Figure S1), suggesting a potential regulatory role in human retinal function. To elucidate the *in vivo* role of YTHDF1, *Ythdf1* KO mice were generated using CRISPR/Cas9 gene-editing technology. The target site was designed within exon 3 and its flanking intron regions (Figure 1A), leading to a 777 bp genomic deletion, which was confirmed by Sanger sequencing (Figure 1A, B). This deletion induced a frameshift deletion (−80 bp) in *Ythdf1* transcripts, introducing a termination codon after the 18th amino acid residue (Supplementary Figure S2A). Founder (F0) mice were crossed with wild-type C57BL/6J mice, and their heterozygous offspring were intercrossed to generate homozygous *Ythdf1* KO mice (*Ythdf1*$^{-/-}$) (Supplementary Figure S2B). PCR genotyping confirmed the specific deletion of exon 3, distinguishing *Ythdf1*$^{-/-}$ mice from *Ythdf1*$^{+/+}$ controls (Supplementary Figure S2C). To validate successful YTHDF1 ablation, retinal protein lyases were extracted from 2-month-old *Ythdf1*$^{+/+}$ and *Ythdf1*$^{-/-}$ mice and subjected to western blot analysis. Results demonstrated a complete loss of YTHDF1 protein in *Ythdf1*$^{-/-}$ retinas (Supplementary Figure S2D, E), confirming efficient genomic excision and protein depletion.

YTHDF1 deficiency impairs visual function and leads to progressive retinal degeneration

To determine the pathological consequences of *Ythdf1* deletion, histological analyses were performed to assess retinal morphology at different ages. At 3 and 5 months, no obvious differences in retinal structure were observed between *Ythdf1*$^{-/-}$ and *Ythdf1*$^{f/f}$ controls (Supplementary Figure S3A, B). Immunostaining for rhodopsin (RHO) (rod outer segment (OS) marker) and NaK ATPase (rod inner segment (IS) marker) in retinal cryosections from 5-month-old mice further confirmed the preservation of intact and well-organized OS structures in rod photoreceptors (Supplementary Figure S3C), indicating that retinal architecture remains unaffected during this period. However, at 8 months of age, degeneration of the OS and ONL became apparent in *Ythdf1*$^{-/-}$ retinas (Figure 1C). At 11 months, this degenerative phenotype significantly worsened, with OS length reduced from 17.35±1.4 mm in controls to 8.34±0.8 mm in *Ythdf1*$^{-/-}$ retinas, accompanied by a 23.3% decrease in ONL thickness near the ON (48.73±1.7 vs. 37.36±0.9 mm, respectively) (Figure 1D). Conversely, no substantial differences in the thickness or cell density of the inner nuclear layer (INL) or ganglion cell layer (GCL) were detected at this time point (Supplementary Figure S4A, B), suggesting that photoreceptors were more susceptible to degeneration than any other retinal neuronal cells following *Ythdf1* deletion. By 14 months, only residual OS structures remained in the *Ythdf1*$^{-/-}$ retina, and ONL thickness was significantly reduced to 4–5 cells per row compared with 10–11 cells per row in controls (Figure 1E). Mild thinning of the INL was observed, along with a 15.1% decrease in GCL cell number (20.5±1.1 vs. 17.4±0.9 mm) (Supplementary Figure S4C, D), indicating widespread retinal degeneration.

To evaluate the functional impact of *Ythdf1* loss, scotopic ERGs were recorded in *Ythdf1*$^{-/-}$ and control mice at 11 months. In accordance with the histological results, *Ythdf1*$^{-/-}$ retinas exhibited substantial reductions in both a- and b-wave amplitudes at all flash intensities compared to controls (Figure 1F, H). The mean amplitudes of the a- and b-waves were reduced by approximately 67% and 53%, respectively (Figure 1H), reflecting severe rod dysfunction. Under photopic conditions, light-adapted ERGs revealed slightly reduced a- and b-wave amplitudes (3 cds/m^2) in *Ythdf1*$^{-/-}$ mice, although these differences did not reach statistical significance (Figure 1G, I). However, 30 Hz flicker ERG amplitudes were 38% lower in *Ythdf1*$^{-/-}$ mice compared to age-matched controls (Figure 1G, I), suggesting mild dysfunction in cone photoreceptors. Collectively, these morphological and functional assessments suggest that *Ythdf1* deletion leads to

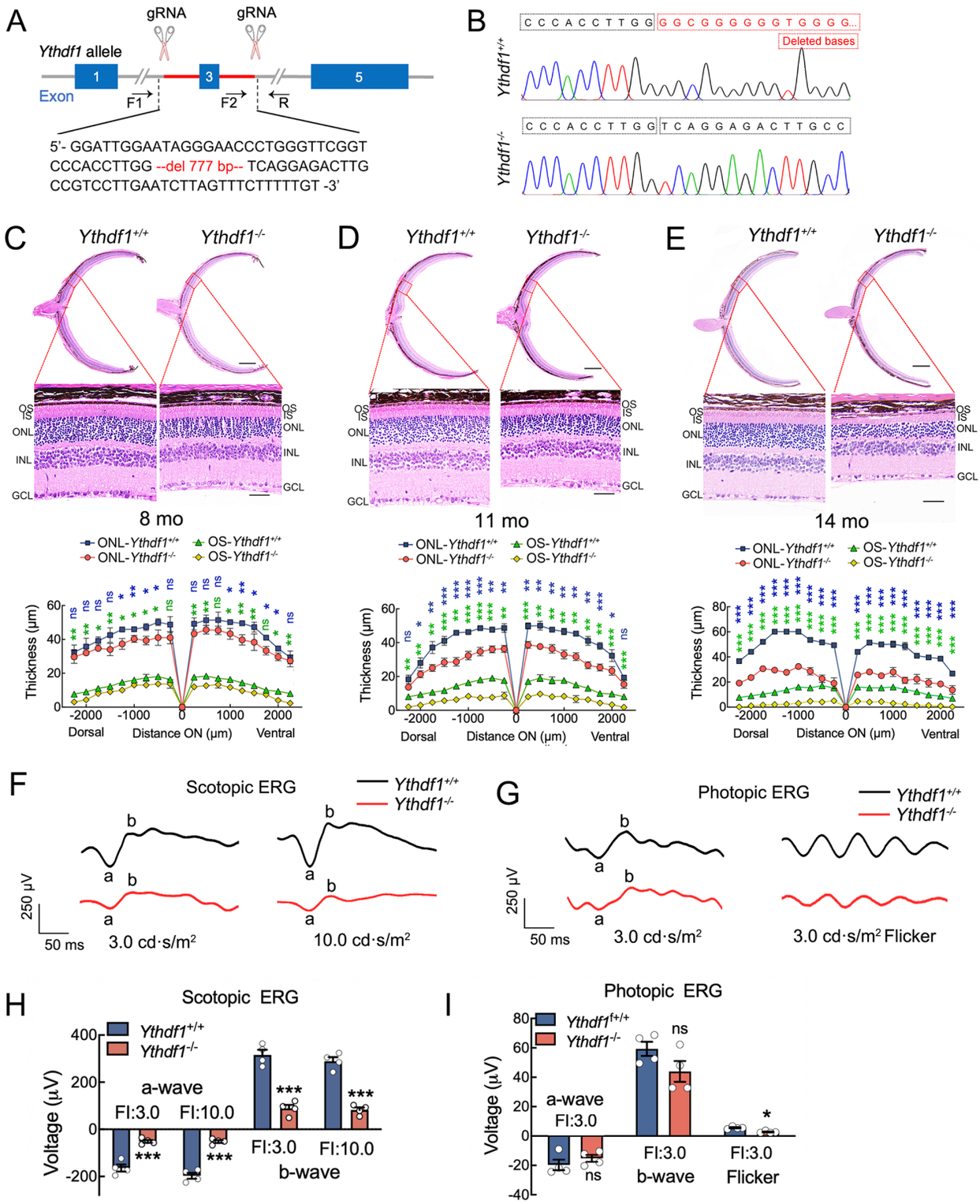

Figure 1 YTHDF1 deficiency impairs visual function and leads to progressive retinal degeneration

A: Schematic representation of the strategy used to generate *Ythdf1*$^{-/-}$ mice. CRISPR/Cas9-mediated deletion of exon 3 in the *Ythdf1* gene resulted in a frameshift mutation and complete loss of *Ythdf1* expression. The 777 bp deleted region is highlighted in red. B: Sanger sequencing confirmation of the 777 bp deletion in *Ythdf1*$^{-/-}$ mice compared to wild-type *Ythdf1*$^{+/+}$ mice. C–E: H&E staining of paraffin-embedded retinal sections from *Ythdf1*$^{-/-}$ and control mice at 8 (C), 11 (D), and 14 months (E). Scale bar: 25 μm. Lower panels show quantification of ONL thickness in *Ythdf1*$^{+/+}$ (*n*=8 per group) and *Ythdf1*$^{-/-}$ (*n*=6 per group) retinas at different ages. Blue asterisks indicate statistical *P*-values for ONL thickness comparisons, while green asterisks represent statistical *P*-values for OS length comparisons. F, G: Representative electroretinogram (ERG) traces recorded under scotopic (F) and photopic (G) conditions at flash intensities (FI) of 3 or 10 cd·s/m^2 from 11-month-old mice. H: Quantification of scotopic a-wave, b-wave amplitudes (*n*=4). I: Quantification of photopic ERG and flicker amplitudes (*n*=4). OS, outer segment; IS, inner segment; ONL, outer nuclear layer; INL, inner nuclear layer; GCL, ganglion cell layer. *: *P*<0.05; **: *P*<0.01; ***: *P*<0.001; ns: Not significant. Data are presented as mean±standard error of the mean (SEM).

retinal degeneration characterized by photoreceptor loss and progressive impairment of both rod- and cone-mediated vision, resembling features of IRD and retinitis pigmentosa (RP).

ScRNA-seq reveals the classification and identity of major retinal cell types

To characterize transcriptomic alterations in individual retinal cell types and investigate structural changes associated with pathological degeneration, scRNA-seq was performed on retinal cells from *Ythdf1*$^{+/+}$ and *Ythdf1*$^{-/-}$ mice at 8 months of age (three retinas from three mice per group). Neural retinas were isolated, dissociated into single-cell suspensions, and subjected to scRNA-seq using the BD Rhapsody scRNA-seq platform (Figure 2A). In total, 15 323 and 13 076 cells were collected from control and *Ythdf1*$^{-/-}$ samples, respectively, with an average of 10 603 reads per cell and 3 024 UMIs per cell. After stringent quality control and filtering using the Seurat package (Butler et al., 2018), 12 827 and 10 218 retinal cells derived from *Ythdf1*$^{+/+}$ and *Ythdf1*$^{-/-}$ mice, respectively, were retained for downstream analysis. Clustering analysis identified 22 transcriptionally distinct retinal cell populations (Supplementary Figure S5). Cell type identities were assigned based on well-established retinal marker genes (Menon et al., 2019), leading to the classification of nine major cell types (Figure 2B–E), including rod photoreceptors (*Pde6a*, *Tulp1*, and *Nr2e3*), cone photoreceptors (*Gnat2*, *Opn1sw*, *Opn1mw*, and *Opn1lw*), retinal ganglion cells (RGCs, *Nefm* and *Slc17a6*), bipolar cells (BCs, *Camk2b*, *Grm6*, *Tmem215*, and *Trpm1*), amacrine cells (ACs, *Gad1* and *C1ql2*), horizontal cells (HCs, *Onecut1*, *Onecut2*, and *Lhx1*), Müller glial cells and astrocytes (*Glul*, *Glu*, and *Apoe*), microglial cells (*C1qa*, *Tmem119*, *Aif1*, and *Cd163*), and vascular endothelial cells (*Adamts9*, *Cd34*, *Cdh5*, and *Rgs5*). Müller glial cells and astrocytes were grouped into a single cluster, likely due to the relatively low number of astrocytes within the retinal cell population. The expression patterns of representative marker genes were visualized using t-SNE plots (Figure 2F). DEGs were ranked based on log2 fold-change values, and the five most significant marker genes for each cell type were selected for visualization (Figure 2G, H). The presence of well-characterized, cell type-specific markers among the top-ranked DEGs validated the accuracy of classification, supporting the reliability of the dataset for further analysis.

Gene expression profiles across retinal cell types

Following the classification of major retinal cell populations, single-cell transcriptomic data were analyzed to characterize the expression patterns of m^{6}A-related genes across different cell types. Broad yet variable expression levels of m^{6}A "writer" genes (*Mettl3*, *Mettl14*, *Wtap*, *Cbll1*, *Nfia*, *Rbm15*, *Zcchc4*, *Zc3h13*, *Mettl4*, *Mettl5*, and *Mettl16*) (Supplementary Figure S6A) and "eraser" genes (*Alkbh5*, *Fto*, and *Alkbh3*) (Supplementary Figure S6B) were observed throughout the retina. Notably, the majority of these genes exhibited high expression in photoreceptors, bipolar cells, and amacrine cells, but low expression in retinal ganglion cells and horizontal cells. For m^{6}A "reader" genes, with the exception of IGF2BP family members, most genes (*Ythdf1*, *Ythdf2*, *Ythdf3*, *Ythdc1*, *Ythdc2*, *Eif3a*, *Hompa2b1*, *Rbmx*, *Hnmpc*, *Prrc2a*, and *Fmr1*) follow a similar distribution pattern as m^{6}A writers and erasers, with enriched expression in photoreceptors, BCs, and ACs (Supplementary Figure S7A, B). Among IGF2BP genes, *Igf2bp2* displayed relatively weak expression in photoreceptors and microglia, while *Igf2bp1* and *Igf2bp3* were barely detectable in any retinal cell type (Supplementary Figure S7A, B). To validate the presence of m^{6}A-related proteins in the retina, lysates from adult wild-type mouse retinas were analyzed via western blotting. Consistent with the transcriptional data, distinct expression of key m^{6}A-related proteins was observed, including core components of the "writer" complex (METTL3, METTL14, and WTAP) (Supplementary Figure S6E), "eraser" enzymes (FTO and ALKBH5) (Supplementary Figure S6E), and a subset of "reader" proteins (YTHDF1-3, YTHDC1-2, and IGF2BP1-3) (Supplementary Figure S7C). These findings suggest a functional role for m^{6}A-related modules in maintaining retinal function and homeostasis.

To assess the effects of *Ythdf1* deletion on retinal cell composition, the proportions of various cell clusters were compared between *Ythdf1*$^{+/+}$ and *Ythdf1*$^{-/-}$ retinas at 8 months. t-SNE visualization of cell distributions showed comparable clustering patterns between genotypes (Figure 2I), indicating no major shifts in overall cell-type composition. However, quantitative analysis revealed a noticeable reduction in rod photoreceptors in *Ythdf1*$^{-/-}$ retinas compared to controls (Figure 2J). To further investigate the molecular consequences of *Ythdf1*$^{-/-}$ deletion, scRNA-seq data were analyzed to identify transcriptional alterations across individual cell types. This cell-type-specific approach allowed the detection of gene expression changes that may otherwise be obscured in bulk RNA sequencing. DEGs were identified in each retinal cell type, with the top 20 up- and down-regulated genes shown in Supplementary Figures S8, S9. GO enrichment analysis of DEGs revealed distinct functional disruptions across retinal cell populations (Supplementary Figures S8, S9; Supplementary Table S3). Notably, genes associated with glutamatergic synapse function and axonal regulation were significantly down-regulated in ACs, BCs, and HCs (Supplementary Figure S8A–C), while DEGs in RGCs were strongly enriched in pathways related to translation and ribosomal function (Supplementary Figure S8D). These findings indicate that YTHDF1 deficiency profoundly alters the molecular landscape of multiple retinal cell types, likely contributing to their dysfunction and degeneration.

***Ythdf1* deficiency leads to rod photoreceptor degeneration and reactive gliosis**

Significant thinning of the ONL (Figure 1C–E) and a reduction in rod photoreceptor clusters (Figure 2I, J) in *Ythdf1*$^{-/-}$ mice prompted further investigation of rod photoreceptor pathophysiology. To assess the impact of YTHDF1 deficiency on protein expression and localization in rod cells, immunofluorescence staining was performed on retinal cryosections using specific antibodies targeting OS proteins, including RHO, protein peripherin 2 (PRPH2), phosphodiesterase-6-β (PDE6B), cGMP-gated cation channel alpha-1 (CNGA1), and GPCR kinase 1 (GRK1), as well as the IS marker NaK ATPase (Figure 3A). Immunofluorescence staining revealed that, despite OS shortening, these proteins remained properly localized within the OS layer of *Ythdf1*$^{-/-}$ mice (Figure 3A), suggesting that OS-residing protein transport from the IS to OS was not impaired. Consistent with the immunohistochemical findings, western blot analysis confirmed a significant reduction in RHO, PRPH2, and GNAT1 protein levels in *Ythdf1*$^{-/-}$ retinas compared to controls

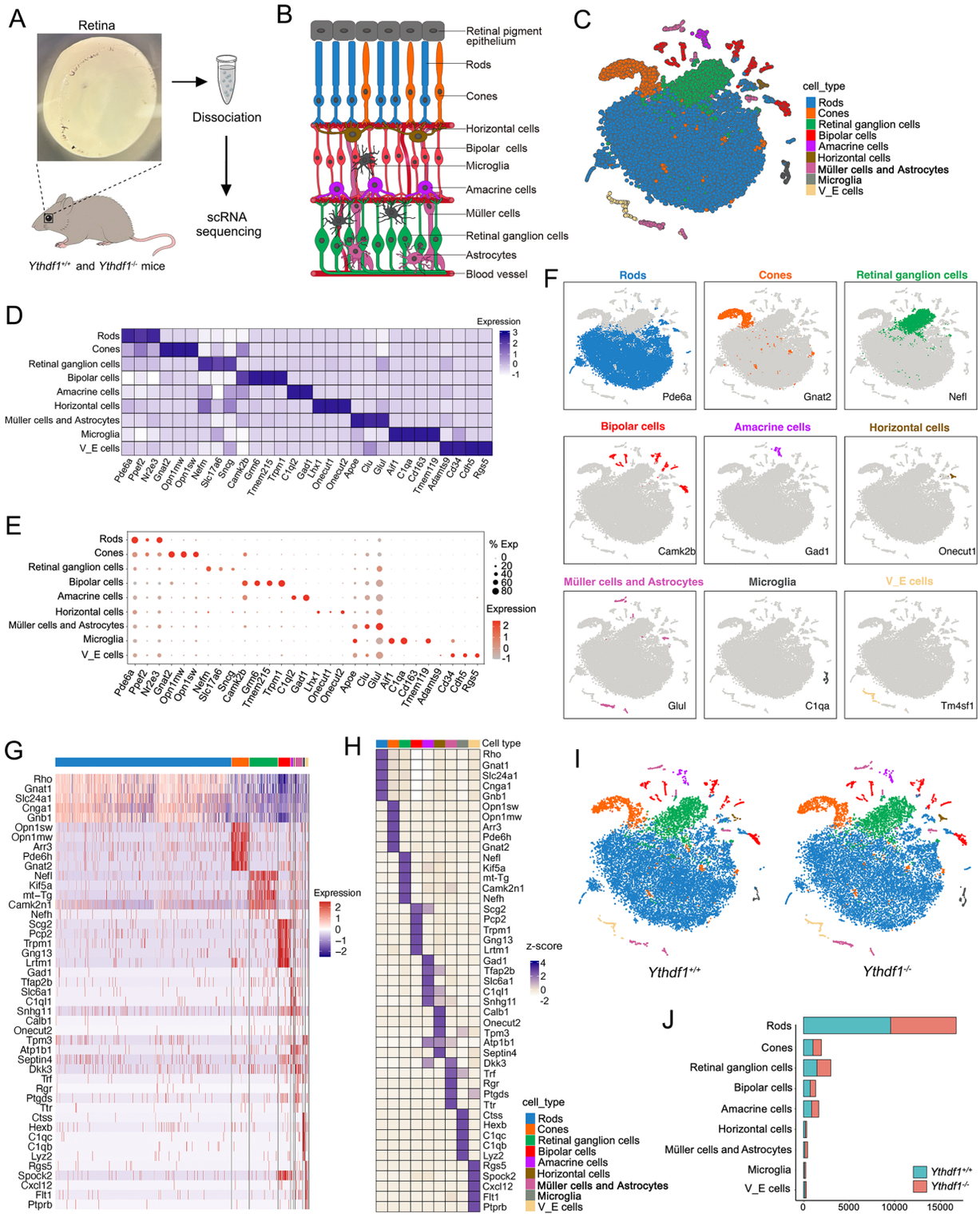

Figure 2 Classification and identification of major retinal cell types using scRNA-seq

A: Schematic overview of sample preparation and scRNA-seq workflow. Retinas from three *Ythdf1*$^{+/+}$ and three *Ythdf1*$^{-/-}$ mice were dissociated into single-cell suspensions and subjected to sequencing. B: Schematic representation of a retinal cross-section, illustrating the major retinal layers and cell types. C: t-distributed stochastic neighbor embedding (t-SNE) visualization of scRNA-seq dataset from adult *Ythdf1*$^{+/+}$ retinas. Cells are colored based on cluster assignments using graph clustering. D: Heatmap showing average expression of well-known marker genes for each major cell type. E: Dot plot showing expression patterns of known cell-type marker genes (columns) across cell clusters (rows). F: t-SNE plots showing expression of selected marker genes representing major retinal cell types. G, H: Heatmap showing relative expression of transcripts with high specificity to individual cell types. H: Imputed gene expression across all cells, and average raw expression of each gene within each cell-type. I: t-SNE plot of total retinal cells isolated from *Ythdf1*$^{+/+}$ and *Ythdf1*$^{-/-}$ retinas, colored by cluster assignments determined using graph clustering. J: Number of *Ythdf1*$^{+/+}$ (blue) and *Ythdf1*$^{-/-}$ (orange) retinal cells per cluster. ONL, outer nuclear layer; INL, inner nuclear layer; OPL, outer plexiform layers; IPL, inner plexiform layers; GCL, ganglion cell layer.

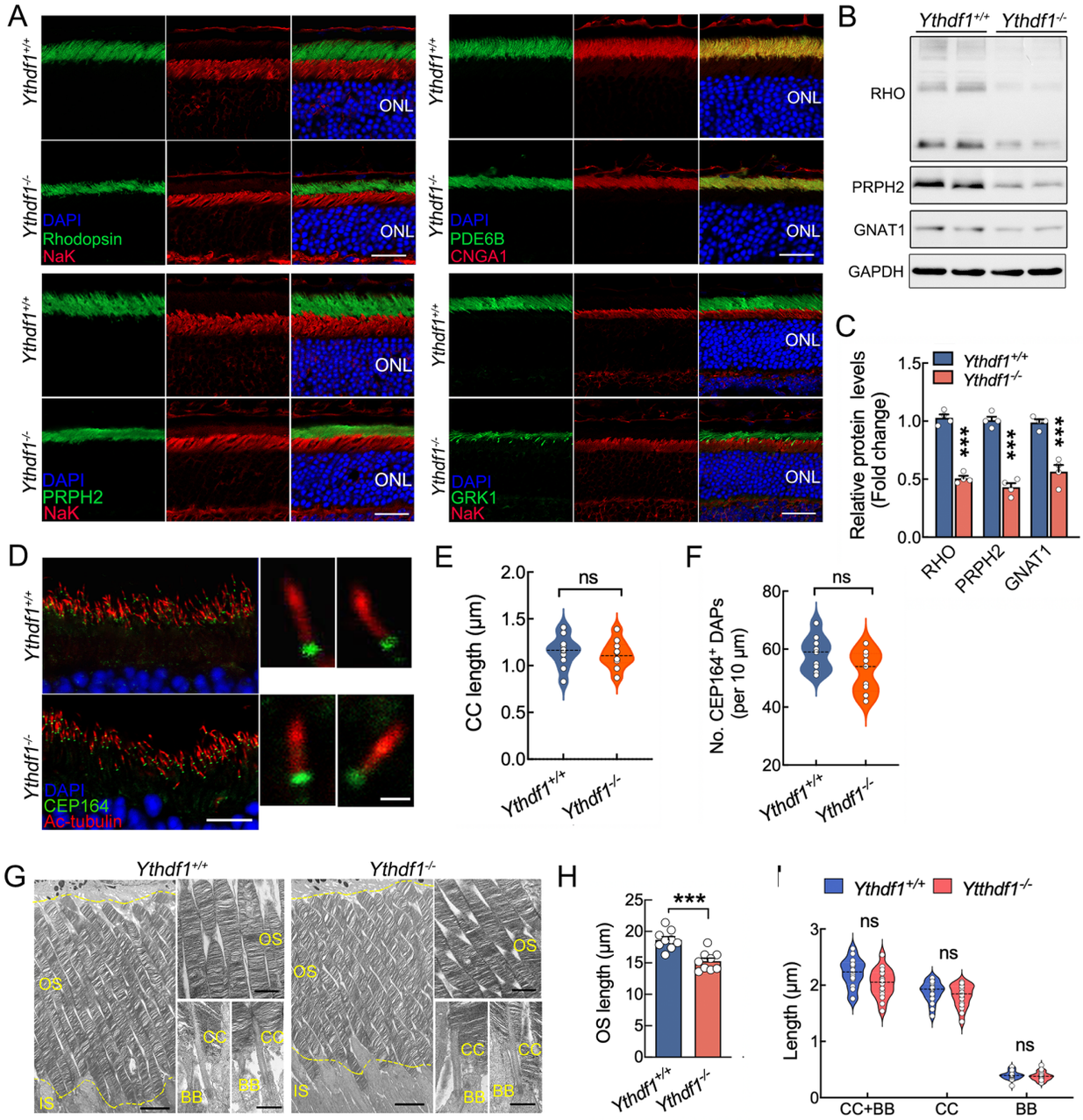

Figure 3 Loss of *Ythdf1* impairs visual function and leads to progressive degeneration of rod cells

A: Immunofluorescence staining of retinal cryosections from 8-month-old *Ythdf1*$^{+/+}$ and *Ythdf1*$^{-/-}$ mice using antibodies against OS markers RHO, PDE6B, PRPH2, and GRK1 and IS marker NaK ATPase (red). Nuclei were counterstained with DAPI. Scale bars: 25 μm. B: Western blot analysis of OS-associated proteins in 8-month-old *Ythdf1*$^{+/+}$ and *Ythdf1*$^{-/-}$ retinas. GAPDH was used as a loading control. At least three independent experiments were performed. C: Quantification of protein expression levels. Expression of each protein was normalized to GAPDH. D: Representative immunofluorescence images of the ciliary marker acetylated α-tubulin (Ac-tubulin) (red) and distal appendage (DAP) marker CEP164 (green) in retinas from 8-month-old mice. Nuclei were counterstained with DAPI (blue). Scale bars: 5 μm. Higher-magnification images of representative ciliary regions are shown on the right. Scale bars: 0.5 μm. E: Quantification of CC length in *Ythdf1*$^{+/+}$ and *Ythdf1*$^{-/-}$ photoreceptors (n=9 from three mice). F: Quantification of CEP164-marked DAPs in *Ythdf1*$^{+/+}$ and *Ythdf1*$^{-/-}$ photoreceptors (n=9 from three mice). G: Representative transmission electron microscopy (TEM) images of photoreceptor OS and ciliary regions in 8-month-old *Ythdf1*$^{+/+}$ and *Ythdf1*$^{-/-}$ mice. Scale bar: 5 μm. Arrows indicate OS and enlarged images of OS discs are shown in the right panel. Scale bars: 2 μm. Higher-magnification images of the ciliary region are shown on the right of each genotype. Scale bars: 500 nm. H: Quantification of OS length in mid-peripheral retina (n=9 from three mice). I: Quantitative analyses of BB and CC lengths between *Ythdf1*$^{+/+}$ and *Ythdf1*$^{-/-}$ photoreceptors (n=14 from three mice). CC, connecting cilium; BB, basal body; OS, outer segment; IS, inner segment; ONL, outer nuclear layer. ***: P<0.001; ns: Not significant. Data are presented as mean±SEM.

(Figure 3B, C), reflecting widespread rod photoreceptor deficits.

Given that METTL14-deficient rods exhibit ciliary deficits (Yang et al., 2022b), the potential involvement of YTHDF1 in ciliary maintenance was examined. Immunofluorescence staining was performed on cryosections from 8-month-old

Ythdf1$^{+/+}$ and *Ythdf1*$^{-/-}$ mice using antibodies against the ciliary marker acetylated α-tubulin (Ac-tubulin) and distal appendage protein (DAP) CEP164 (Figure 3D). However, no significant differences were observed in mean cilium length (1.15±0.07 μm vs 1.12±0.03 μm, P=0.654, n=9; Figure 3E) or CEP164-marked DAPs (58.44±3.14 vs 52.22±6.12, P=0.063, n=9; Figure 3F) between groups. Ultrastructural analysis via transmission electron microscopy further confirmed well-organized OS disc morphology in *Ythdf1*$^{-/-}$ retinas, despite a notable reduction in OS length (Figure 3G, H). Additionally, no significant differences in connecting cilium (CC) or basal body (BB) length were detected between *Ythdf1*$^{-/-}$ (CC, 1.87± 0.09 μm; BB, 0.39±0.04 μm) and control rods (CC, 1.81± 0.08 μm; BB, 0.38±0.05 μm) (Figure 3I), indicating that ciliary structure was not disrupted by YTHDF1 loss.

Consistent with scRNA-seq data showing an increase in Müller glial cells (Figure 2I, J), immunostaining with glial fibrillary acidic protein (GFAP) antibody revealed a pronounced up-regulation of GFAP expression across the outer plexiform layer (OPL), INL, inner plexiform layer (IPL), and GCL of degenerating *Ythdf1*$^{-/-}$ retinas compared to controls (Supplementary Figure S10A). Western blot analysis further confirmed a significant increase in GFAP protein levels in *Ythdf1*$^{-/-}$ retinas (Supplementary Figure S10B, C). These findings indicate that Müller glial cell activation is a prominent feature of YTHDF1-deficient retinas, likely serving as a reactive response to photoreceptor degeneration (Yang et al., 2019, 2021).

Cone OS shortening without pronounced cone cell loss in *Ythdf1*$^{-/-}$ retinas

To assess the impact of YTHDF1 deficiency on cone photoreceptors, retinal cryosections from 8-month-old *Ythdf1*$^{+/+}$ and *Ythdf1*$^{-/-}$ mice were immunolabeled with cone arrestin (cArr) to visualize cone cells (Figure 4A). Quantification of cone density across the retina revealed no significant differences between genotypes (Figure 4A, B), indicating that YTHDF1 deletion did not result in significant cone loss at this stage. To further investigate pathological changes in cone structure, retinal flat mounts were co-immunostained with an M-opsin antibody to label the cone OS and Alexa Fluor-594-conjugated peanut agglutinin (PNA) to label the cone matrix sheaths of all cone subtypes (Figure 4C). Given that M-opsin-expressing cones are largely concentrated in the dorsal retina, with few M-opsin-positive cones in the ventral retina (Eldred et al., 2020), analyses were restricted to the dorsal retina. Measurements revealed a slight decrease in OS length in *Ythdf1*$^{-/-}$ cones, while M-cone density remained unchanged (Figure 4D, E), corroborating findings from cArr immunolabeling. Further immunostaining of retinal sections with M-opsin and Alexa Fluor-594-tagged PNA confirmed the presence of shortened and structurally aberrant cone OS in *Ythdf1*$^{-/-}$ retinas compared to controls (Figure 4F), suggesting the onset of cone cell degeneration. Thus, the mild degeneration observed in cone photoreceptors suggest that the significant ONL thinning in *Ythdf1*$^{-/-}$ retinas is primarily driven by extensive rod photoreceptor loss rather than cone degeneration.

Transcriptome-wide identification of YTHDF1 targets in retinal rod cells

To elucidate the molecular mechanisms underlying *Ythdf1*-associated photoreceptor degeneration, photoreceptor cells were re-clustered into rods and cones based on the expression of RHO and arrestin-3 (Arr3), respectively. Cone cells were further subtyped into S-cones, identified by S-opsin expression, and M-cones, identified by M-opsin expression (Figure 5A, B). Comparative analysis between *Ythdf1*$^{-/-}$ and control rod cells identified 122 DEGs (fold-change≥1.5 or ≤ 1/1.5; adjusted P<0.05) (Figure 5C; Supplementary Table S4), consisting of 76 up-regulated and 46 down-regulated genes. GO enrichment analysis of these genes revealed a significant down-regulation of pathways associated with visual perception and photoreceptor outer and inner segment (Figure 5D, highlighted in red; Supplementary Table S3), underscoring the essential role of YTHDF1 in maintaining normal rod photoreceptor function. For cone photoreceptors, DEGs were identified in total cone populations and in each cone subtype, with the top 20 up- and down-regulated genes presented in Supplementary Figure S10. GO analysis of DEGs revealed multiple enriched pathways in both total (Supplementary Figure S11A) and each cone types (Supplementary Figure S11B, C), such as downregulated visual perception (Supplementary Figure S11A) and translation pathway (Supplementary Figure S11B, C), as well as upregulation of regulation of apoptotic process (Supplementary Figure S11C), suggesting that cone cells were likely undergoing degenerative impairment.

As a crucial m^{6}A reader, YTHDF1 recognizes and selectively binds m^{6}A-methylated mRNAs, facilitating their translation efficiency (Wang et al., 2015). To identify YTHDF1-bound mRNAs in the retina, anti-YTHDF1 RIP followed by RIP-seq was performed on wild-type retinal lysates (Figure 5E). RIP-seq identified 908 candidate YTHDF1 targets (Supplementary Figure S12A; Supplementary Table S5), 92.93% of which were mRNAs (Figure 5F). Functional enrichment analysis revealed that these YTHDF1-associated transcripts were involved in diverse biological pathways (Supplementary Figure S12B–D and Table S6). Analysis of binding-site distribution showed that most of these sites were located in protein-coding transcripts and highly enriched in CDS (62.3%) and 3' untranslated regions (3'UTR) (27.7%) (Figure 5G). Motif analysis identified CGGACUG as the most enriched binding sequence (Figure 5H), consistent with known m^{6}A-targeted sequences. To further investigate the functional significance of YTHDF1 target transcripts, RIP-seq data were integrated with scRNA-seq DEGs from each retinal cell type, resulting in a subset of potential YTHDF1-regulated targets across various retinal populations (Supplementary Table S7). Given that m^{6}A modification plays a crucial role in retinal function, publicly available MeRIP-seq data (SRA database: PRJNA756938) obtained from the retinas of METTL14 rod-conditional KO mice (Yang et al., 2022b) were analyzed, identifying 5 566 m^{6}A peaks across 1 678 genes with significantly reduced m^{6}A modifications in METTL14-deficient retinas (Supplementary Table S8).

As *Ythdf1* deletion resulted in progressive retinal degeneration and photoreceptor deficits reminiscent of human RP/IRD pathologies, potential correlations between YTHDF1 target genes and RP/IRD-associated genes were explored. A curated list of 122 non-syndromic RP/IRD-related genes (Supplementary Table S9) was obtained from the RetNet database (https://sph.uth.edu/retnet). Venn diagram analysis of common targets in RIP-seq, MeRIP-seq, and RP/IRD-related genes identified three overlapping RP/IRD-related genes (*Tulp1*, *Cngb1*, and *Dhx38*) that were bound by YTHDF1 and tagged with m^{6}A. These genes showed

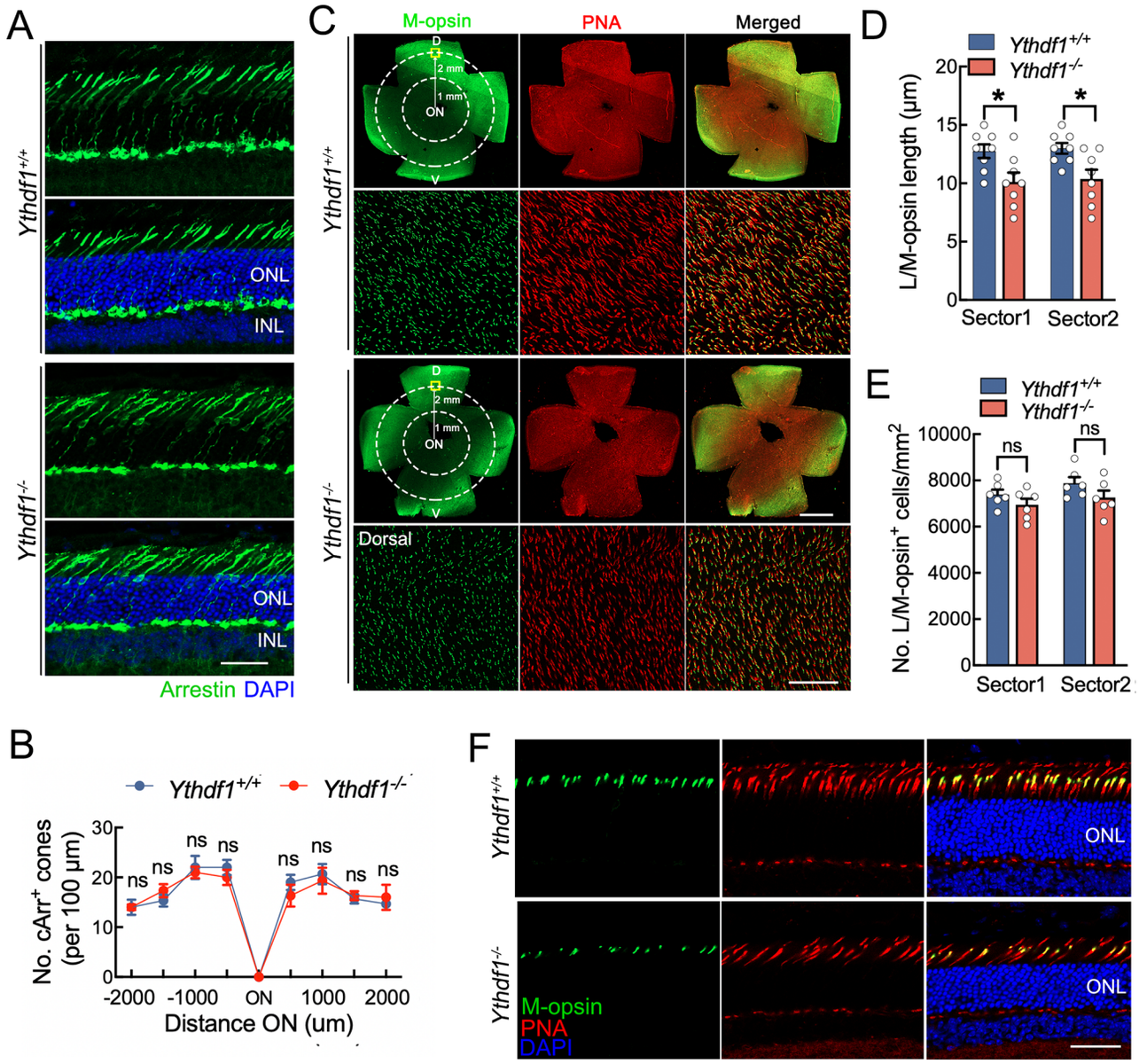

Figure 4 Mild cone photoreceptor phenotype in *Ythdf1*$^{-/-}$ retinas

A: Representative immunofluorescence images of cone arrestin (green) in retinas from 10-month old *Ythdf1*$^{+/+}$ and *Ythdf1*$^{-/-}$ mice. Nuclei were counterstained with DAPI (blue). Scale bars: 25 μm. B: Quantification of cone arrestin-positive cells per 500 μm field in *Ythdf1*$^{+/+}$ and *Ythdf1*$^{-/-}$ retinas (*n*=6). Each cone population was counted in the inferior and superior retinal quadrant, starting −2 500 μm from the ora serrata towards the optic disc at 500 μm intervals. C: Immunostaining of flat-mounted retinas from 10-month-old *Ythdf1*$^{+/+}$ and *Ythdf1*$^{-/-}$ mice using M-opsin and PNA markers. Scale bars: 50 μm. Representative images from the dorsal retinal quadrant are shown in the lower panel. Scale bars: 25 μm. D, E: Quantification of M-opsin-positive OS length (D) and cone density per 1 mm^2 field (E) in *Ythdf1*$^{+/+}$ and *Ythdf1*$^{-/-}$ retinas (*n*=8 in D and *n*=6 in E). Schematic of retinal flat mount indicates the two sectors (radii: 1 and 2 mm) used for cone quantification. F: Immunofluorescence staining of retinal cryosections from 10-month-old mice labeled with PNA and M-opsin. Nuclei were counterstained with DAPI. Scale bars: 25 μm. ONL, outer nuclear layer; INL, inner nuclear layer. *: *P*<0.05; **: *P*<0.01; ns: Not significant. Data are presented as mean±SEM.

decreased m^{6}A levels upon METTL14 elimination (Figure 5I), while their mRNA levels remained unchanged in *Ythdf1*$^{-/-}$ retinas compared to controls, as confirmed by scRNA-seq (Figure 5J). Of note, *Tulp1*, *Cngb1*, and *Dhx38* are well-known RP-associated genes with established roles in retinal physiology and photoreceptor survival (Grossman et al., 2009; Hagstrom et al., 1999; Latif et al., 2018; Nassisi et al., 2021; Obuća et al., 2022; Petersen-Jones et al., 2018). Given their functional significance, subsequent analyses focused on elucidating the regulatory role of YTHDF1 in these target genes.

YTHDF1 facilitates the translation of m^{6}A-methylated *Tulp1* and *Dhx38* in mouse retinas

To elucidate the mechanism by which YTHDF1 regulates *Tulp1*, *Cngb1*, and *Dhx38* expression in the retina, their transcriptomic profiles were compared between *Ythdf1*$^{+/+}$ and *Ythdf1*$^{-/-}$ retinas. t-SNE visualization showed that *Tulp1* and *Cngb1* were highly expressed in both rods and cones, while *Dhx38* exhibited lower expression levels (Figure 6A). Dot plot analysis confirmed that *Tulp1* was highly expressed across all three photoreceptor subclusters, whereas *Cngb1* was less abundant in S-cones, and *Dhx38* was largely absent from all

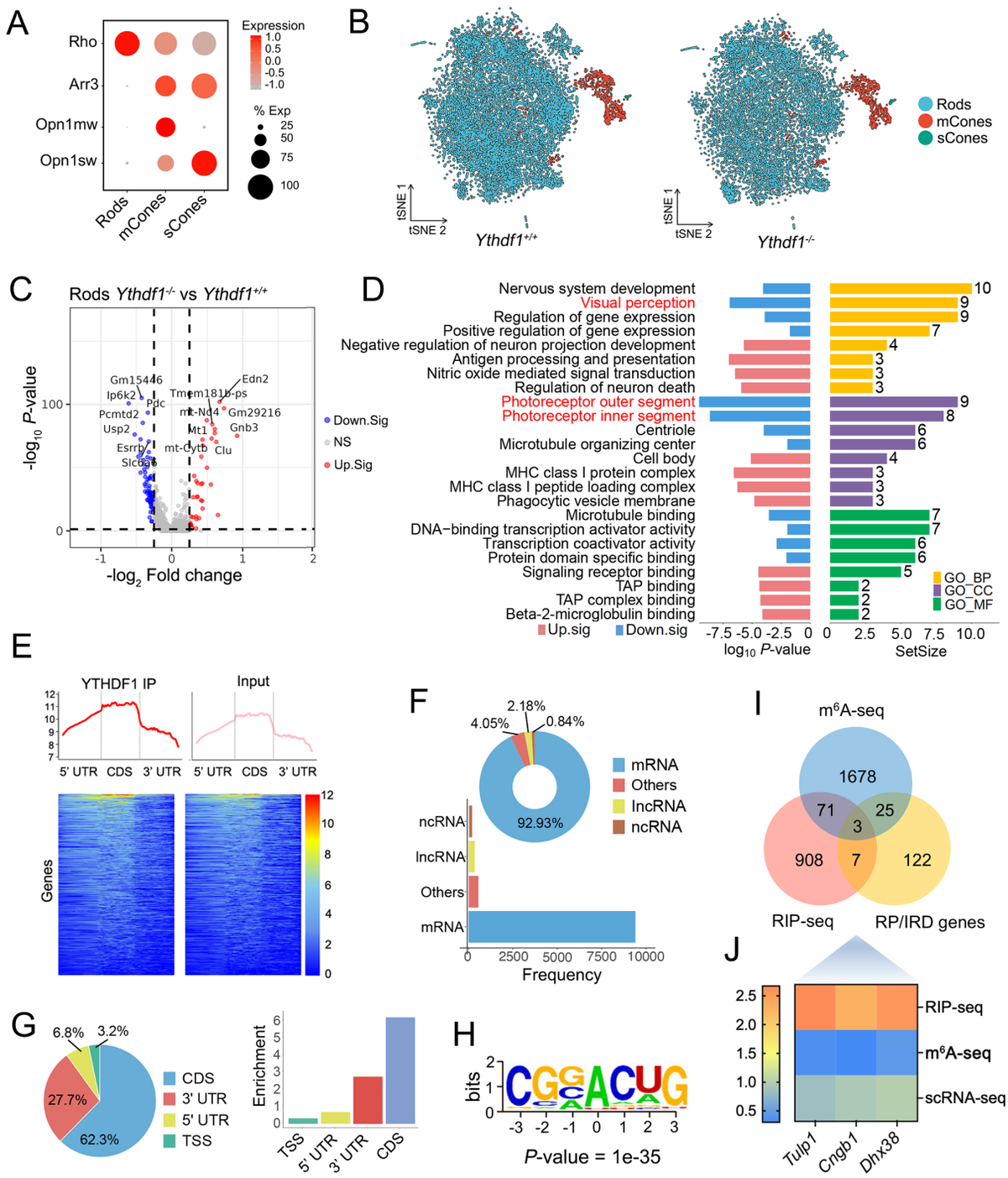

Figure 5 Transcriptome-wide identification of YTHDF1 targets in retinal rod cells

A: Dot plot showing expression of selected marker genes distinguishing rods, M-cones, and S-cones. Dot size represents percentage of cells within a cluster expressing a given gene, while color intensity represents the average expression level within expressing cells. B: *t*-SNE visualization of single-cell clusters. Dots represent individual cells, color-coded by cluster assignment. C: Volcano plots displaying differentially expressed mRNAs between *Ythdf1*$^{+/+}$ and *Ythdf1*$^{-/-}$ rods, with statistical significance (fold changes≥1.5 and *P*<0.05). D: Pathway analysis and GO term enrichment for DEGs categorized into biological process (BP), cellular component (CC) and molecular function (MF). Down-regulated gene-associated terms are indicated in blue, and up-regulated gene-associated terms are shown in red. E: Distribution of RIP peaks across mRNA transcripts in *Ythdf1*$^{+/+}$ retinas, categorized into 5' UTRs, CDS, and 3' UTRs. F: Distribution of YTHDF1-bound transcripts identified by RIP-seq. G: Distribution (left) and enrichment (right) of YTHDF1-binding sites across different transcript regions. Enrichment was determined by normalizing the proportion of m^{6}A peaks to the relative length of each transcript region. H: Consensus sequence motifs of YTHDF1-binding sites detected through HOMER motif analysis of RIP-seq data. I: Venn diagram of differentially expressed m^{6}A genes (identified by m^{6}A-seq), YTHDF1-conjugated transcripts (identified by RIP-seq), and RP/CRD related genes. Three genes were selected based on their overlap. RIP-seq data were acquired from the present study, while m^{6}A-seq data of *Mettl14* floxed and *Mettl14* rod KO mouse retinas were obtained from SRA datasets (PRJNA756938). RP/CRD-related genes were obtained from the RetNet database (https://sph.uth.edu/retnet/). Detailed gene sets for RIP-seq and m^{6}A-seq are listed in Supplementary Table S5 and S8, respectively. J: Heatmap of three overlapping genes identified in (I).

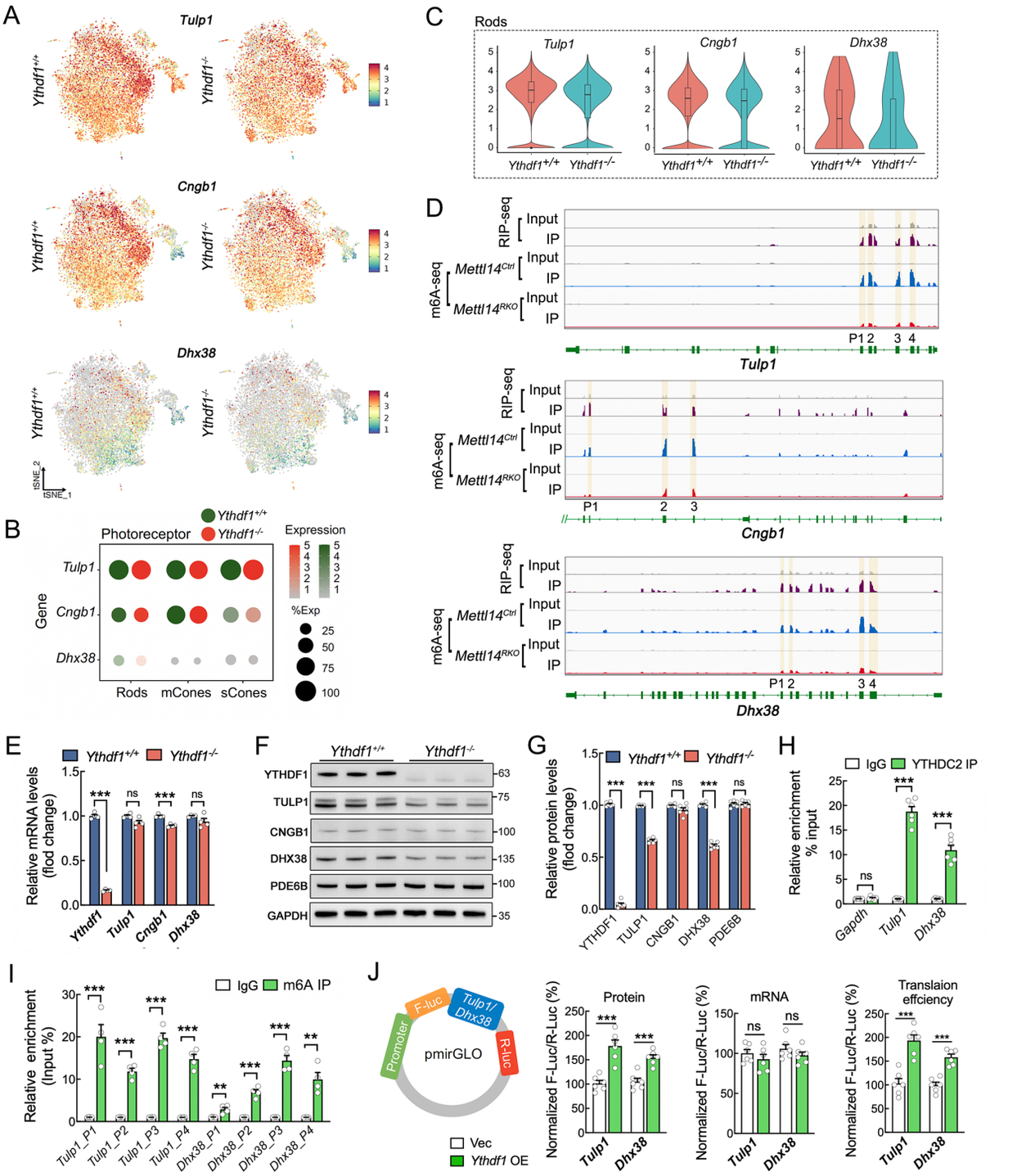

Figure 6 YTHDF1 promotes translation of m^{6}A-methylated *Tulp1* and *Dhx38* in retinas

A: *t*-SNE plots showing expression levels of selected genes in *Ythdf1*$^{+/+}$ and *Ythdf1*$^{-/-}$ mouse retinas. B: Dot plots showing expression differences of selected genes between *Ythdf1*$^{+/+}$ and *Ythdf1*$^{-/-}$ photoreceptors. C: Violin plots showing expression levels of selected genes in rod photoreceptors of *Ythdf1*$^{+/+}$ and *Ythdf1*$^{-/-}$ mice. D: Integrative Genomics Viewer (IGV) tracks displaying m^{6}A peaks and YTHDF1-binding sites among selected genes based on m^{6}A-seq and YTHDF1 RIP-seq. RIP-seq data were acquired from the present study, while m^{6}A-seq data of *Mettl14* floxed (*Mettl14*^{Ctrl}) and *Mettl14* rod KO (*Mettl14*^{RKO}) mouse retinas were obtained from SRA datasets (PRJNA756938), as previously published. E: RT-qPCR validation of scRNA-seq results for indicated genes (n=4). F, G: Representative immunoblots (F) and quantification (G) of protein levels in retinas from 8-month-old mice. Protein expression levels were normalized to GAPDH (n=6). H: RIP-qPCR analysis confirming binding between YTHDF1 and indicated transcripts in mouse retinal cells (n=6). I: MeRIP-qPCR validation of m^{6}A enrichment at multiple sites (highlighted in Figure 6D) within selected gene transcripts. J: Wild-type (WT) or YTHDF1 overexpression (OE) HEK-293T cells were transfected with pmirGLO-*Tulp1* reporter for 24 h, followed by dual-luciferase assay. Protein, mRNA, and translation efficiencies were determined (n=6), with translation efficiency of *Tulp1* defined as the quotient of reporter protein production (F-Luc/R-Luc) divided by mRNA abundance. *: P<0.05; **: P<0.01; ***: P<0.001. ns: Not significant. Data are presented as mean±SEM.

cone subtypes (Figure 6B). Notably, no significant differences in the transcript levels of these genes were detected between *Ythdf1*$^{+/+}$ and *Ythdf1*$^{-/-}$ retinas (Figure 6B). Since *Tulp1*, *Cngb1*, and *Dhx38* were expressed in rod photoreceptors (Figure 6A, B), their specific expression levels were compared between the *Ythdf1*$^{+/+}$ and *Ythdf1*$^{-/-}$ groups. This analysis revealed no significant difference in expressions in the two groups (Figure 6C), suggesting that YTHDF1 deficiency does not influence the mRNA levels of these genes. To further investigate YTHDF1-mediated regulation, YTHDF1 RIP-seq data were integrated with m^{6}A profiling using Integrative Genomics Viewer (IGV). Results demonstrated a strong overlap between YTHDF1-binding sites and m^{6}A peaks within *Tulp1*, *Cngb1*, and *Dhx38* transcripts (Figure 6D). Notably, several CDS regions exhibited both significantly reduced m^{6}A methylation and enriched YTHDF1 binding (Figure 6D, highlighted).

To explore the regulatory effects of YTHDF1 on its target transcripts, RT-qPCR was performed. While *Cngb1* exhibited a slight reduction in *Ythdf1*$^{-/-}$ retinas, no significant differences in the transcriptional levels of *Tulp1* and *Dhx38* were observed (Figure 6E). In contrast, western blot analysis revealed a substantial reduction in TULP1 and DHX38 protein expression levels in *Ythdf1*$^{-/-}$ retinas at 5 months of age, a stage at which retinal structure remained largely intact. However, CNGB1 protein expression remained unchanged (Figure 6F, G). To determine whether reduced TULP1 and DHX38 levels resulted from photoreceptor degeneration rather than a direct effect of YTHDF1 deficiency, the expression of PDE6B, a key phototransduction protein, was examined. PDE6B levels remained unchanged between *Ythdf1*$^{+/+}$ and *Ythdf1*$^{-/-}$ retinas (Figure 6F, G), confirming that the observed reductions in TULP1 and DHX38 were not secondary to photoreceptor loss but rather a direct consequence of YTHDF1 depletion. Consistently, TULP1 and DHX38 protein levels, along with CNGB1, were further reduced in the retinas of 8-month-old *Ythdf1*$^{-/-}$ mice (Supplementary Figure S13), correlating with progressive retinal degeneration. These findings indicate that YTHDF1 regulates TULP1 and DHX38 protein expression without altering their transcript abundance, suggesting a translational regulatory mechanism.

To confirm YTHDF1 binding specificity, RIP-qPCR was performed using an anti-YTHDF1 antibody, revealing an 18-fold and 11-fold enrichment of *Tulp1* and *Dhx38* transcripts, respectively, compared to IgG controls (Figure 6H). Detailed IGV analysis demonstrated that multiple YTHDF1-binding regions in *Tulp1* and *Dhx38* mRNA exhibited reduced m^{6}A peaks upon METTL14 deletion (Figure 6D, highlighted), with m^{6}A methylation of these peaks further validated by MeRIP-qPCR (Figure 6I). Considering that YTHDF1 deficiency decreased TULP1 and DHX38 protein levels without affecting their mRNA abundance (Figure 6E–G) and given the key role of YTHDF1 in mRNA translation, we hypothesized that the observed protein reductions resulted from impaired translation efficiency. To test this, firefly luciferase reporter plasmids containing the CDS regions of *Tulp1* and *Dhx38* (*pmirGLO-Tulp1-CDS* and *pmirGLO-Dhx38-CDS*, respectively) were generated (Figure 6J). Dual-luciferase reporter assays demonstrated that YTHDF1 overexpression significantly improved the translation efficiency of *Tulp1* and *Dhx38* (Figure 6J), confirming its role in promoting translation. Collectively, these observations suggest that YTHDF1 facilitates the translation of *Tulp1* and *Dhx38* by selectively recognizing and binding the m^{6}A-modified CDS regions in their transcripts.

DISCUSSION

Mounting evidence highlights the critical role of m^{6}A modification in neuronal development and disease pathogenesis (Livneh et al., 2020). We previously demonstrated the importance of METTL14-mediated m^{6}A methylation in retinal photoreceptor function (Yang et al., 2022b), with subsequent studies reporting the involvement of m^{6}A reader protein-coding genes *Ythdf1*, *Ythdf2*, and *Ythdf3* in retinal neurogenesis, suggesting functional redundancy among YTHDFs in both cortical and retinal neurogenesis (Niu et al., 2022a). However, the role of m6A reader proteins —including YTHDF1, YTHDF2, YTHDF3, YTHDC1, and YTHDC2—in maintaining mature retinal function remains unclear.

YTHDF1 is a well-characterized translational enhancer of m^{6}A-modified mRNAs. Different from its role in neurogenesis, our study revealed photoreceptor dysfunction and retinal degeneration after *Ythdf1* deletion in mature retinas, highlighting its essential role in preserving visual function. Integrative analyses, including snRNA-seq, RIP-seq, and previously published MeRIP-seq, identified *Tulp1* and *Dhx38* as direct YTHDF1 targets in the retina. Mutations in TULP1 have been linked to autosomal recessive Leber congenital amaurosis, early-onset RP, and late onset cone-rod dystrophy (Banerjee et al., 1998; Gu et al., 1998; Hagstrom et al., 1998; Knowles et al., 1994). Animal models have indicated that TULP1 is also involved in RHO localization (Hagstrom et al., 1999, 2001; Jia et al., 2022). Similarly, DHX38, a spliceosome-associated RNA helicase, is associated with early-onset RP (Ajmal et al., 2014; Latif et al., 2018), with pathogenic mutations affecting the splicing of key retinal genes such as *FSCN2* and *RHO* (Obuća et al., 2022). Interestingly, both *Tulp1* and *Dhx38* mutations are associated with early onset photoreceptor degeneration in humans and mice. However, in *Ythdf1* KO mice, the retinal degeneration phenotype was relatively mild and progressive, with no overt structural abnormalities detected until 8 months of age (Figure 1C–E). Western blot analysis revealed that TULP1 and DHX38 protein levels were reduced by approximately 50% in *Ythdf1*$^{-/-}$ retinas compared to controls (Figure 6F, G), likely mirroring a double-heterozygous KO effect. Notably, heterozygous *Tulp1* mutation carriers (heterozygotes) are typically asymptomatic and *Tulp1*$^{+/-}$ mice exhibit normal retinal morphology without significant degeneration (Hagstrom et al., 1999; Mataftsi et al., 2007). Similarly, heterozygous DHX38 mutations produce minimal to no detectable retinal dysfunction (Ajmal et al., 2014). These findings suggest that partial loss of *Tulp1* and *Dhx38* in *Ythdf1*$^{-/-}$ retinas may contribute to the slower progression of retinal degeneration. Mechanistically, YTHDF1-mediated translational regulation of *Tulp1* and *Dhx38* was shown to be dependent on m^{6}A modification of CDS regions, providing the first evidence that m^{6}A readers regulate protein translation in mature retinal photoreceptors. Hence, these findings expand current understanding of m^{6}A-regulated retinal function and highlight the need for further investigations to clarify the specific roles and mechanisms of different m^{6}A readers in retinal maintenance and disease.

Beyond *Tulp1* and *Dhx38*, YTHDF1 likely regulates the translation of many other target proteins across different retinal cell types, as evidenced by the observed loss of RBCs,

ACs, and HCs in *Ythdf1*$^{-/-}$ retinas (Figure 2I, J). While chronic rod photoreceptor degeneration can indirectly contribute to the secondary loss of other retinal neurons, the relatively mild rod degeneration phenotype observed in 8-month-old *Ythdf1*$^{-/-}$ mice suggests that the reduction in RBCs, ACs, and HCs at this stage is more likely a direct consequence of YTHDF1 loss rather than a downstream effect of rod degeneration. Future studies using conditional *Ythdf1* KO models in specific retinal cell types will be necessary to delineate its precise roles in non-photoreceptor cells. Our comprehensive scRNA-seq dataset from YTHDF1 pan-KO retinas, combined with YTHDF1 RIP seq data (Supplementary Table S7), provides a valuable resource for investigating the molecular consequences of YTHDF1 loss and identifying additional YTHDF1-regulated targets. Importantly, the scRNA-seq results (Supplementary Figure S7) further revealed that multiple m^{6}A-reader proteins, including *Ythdf1*, *Ythdf2*, *Ythdf3*, *Ythdc1*, *Ythdc2*, *Eif3a*, *Hompa2b1*, *Rbmx*, *Hnmpc*, *Prrc2a*, and *Fmr1*, were widely expressed in the retina, albeit with varying abundance across distinct cell types. Western blot analysis of adult mouse retina lysates confirmed differential expression patterns of key m^{6}A-related proteins, including “reader” proteins (YTHDF1-3, YTHDC1-2, and IGF2BP1-3) (Supplementary Figure S7C). These findings suggest that multiple m^{6}A readers likely collaborate to regulate retinal function and homeostasis. Supporting this, our recent multi-omics analysis demonstrated that YTHDC2 plays an active role in retinal function by selectively recognizing and binding to m^{6}A-modified *Ppef2*-CDS and *Pde6b*-5’ UTRs, thereby enhancing their translation in an m^{6}A-dependent manner (Yang et al., 2024). Additionally, previous research has shown that retinal neurogenesis defects only emerge when YTHDF1, YTHDF2, and YTHDF3 are simultaneously deleted, while single *Ythdf1* KO has no observable impact on retinal development, indicating functional redundancy among these m^{6}A effectors (Niu et al., 2022a). Our current findings support this conclusion, as *Ythdf1* KO mice displayed normal retinal morphology at 3 months of age (Supplementary Figure S3). Despite this structural preservation in early life, GO analysis of DEGs identified significant enrichment in developmental pathways across multiple retinal cell types (Supplementary Figures S8, S9), possibly reflecting the functional redundancy among m^{6}A readers. This redundancy can occur in three distinct ways: a single effector may regulate different targets across multiple cell types, several m^{6}A effectors may function simultaneously in one cell type, or different readers may exert dominant roles at different developmental stages. The enrichment of development-related pathways in GO analysis suggests that YTHDF1 likely contributes to retinal function in adulthood, potentially acting in collaboration with other m^{6}A readers. Notably, many genes within these pathways are essential for retinal maintenance, indicating that m6A-mediated regulation persists beyond neurodevelopment and plays a role in retinal homeostasis. Our previous studies also demonstrated that m6A modification is critical for cone photoreceptor survival, as evidenced by significant cone degeneration in METTL14-deficient mice. In contrast, although *Ythdf1* deficiency led to severe rod degeneration, cone photoreceptors exhibited only mild structural abnormalities, characterized by shortened OS without substantial cone cell loss (Figure 4). These findings suggest that additional m^{6}A readers likely contribute to cone photoreceptor maintenance. Consequently, further investigations are expected to uncover the specific molecular mechanisms and target genes underlying the regulatory function of related m^{6}A readers in the retina.

Significant progress has been made in identifying the genetic causes of IRDs, with over 280 disease-associated genes discovered through whole-exome and whole-genome sequencing (RetNet: https://sph.uth.edu/retnet/). Despite these advances, a considerable proportion of individuals (30%–40%) remain without a definitive genetic diagnosis, even after extensive genetic analysis. This diagnostic gap continues to present major challenges for clinical management and further research. Recent studies suggest that epigenetic modifications, including DNA methylation, RNA modifications, and histone modifications, contribute to the pathogenesis of various human diseases (Li et al., 2019). Emerging evidence underscores the importance of epigenetic regulators in both neural retinal development and homeostasis. In the current study, *Ythdf1* KO mice exhibited late-onset, progressive retinal degeneration, characterized by diminished ERG response and reduced ONL thickness (Figure 1), mirroring key pathological features of human IRDs. Further investigation revealed that *Ythdf1* deficiency led to compromised TULP1 and DHX38 protein expression due to defects in translation regulation, ultimately resulting in visual dysfunction and progressive retinal degeneration. These findings identify a previously unrecognized regulatory mechanism through which the m^{6}A reader protein YTHDF1 maintains retinal neuronal function and survival. As noted, the limited understanding of the molecular mechanisms underlying IRDs has posed significant challenges to the development of effective treatments for progressive retinal dystrophies. While adeno-associated virus (AAV)-based gene therapies have advanced significantly, their application to IRDs remains constrained by several limitations, including target specificity, immune responses, and long-term efficacy. In contrast, targeting m^{6}A modifications represents an innovative therapeutic strategy for IRDs, with the potential to mitigate disease onset and/or progression by modulating aberrant m^{6}A methylation. However, the precise therapeutic targets of m^{6}A-modifying enzymes in retinal diseases remain largely unexplored. This study highlights the role of YTHDF1 in IRD pathogenesis via the regulation of *Tulp1* and *Dhx38*, providing insight into the broader impact of m6A-mediated translation control in retinal function. Further research is warranted to elucidate the complex mechanisms of m^{6}A modulation in the retina, paving the way for broad-spectrum epigenetic therapies and advanced treatment strategies for IRDs.

In summary, this study revealed that loss of *Ythdf1* resulted in impaired visual function and progressive retinal degeneration in mice, highlighting the essential role of YTHDF1 in retinal neuronal maintenance. ScRNA-seq provided a comprehensive transcriptomic landscape, revealing cell-type-specific molecular alterations in *Ythdf1*-deficient retinas. In rod photoreceptors, YTHDF1 regulated retinal function by specifically recognizing and binding to m^{6}A-modified *TULP1* and *DHX38* CDS sites near the stop codon, primarily via its YTH domain, thereby promoting their translation in an m^{6}A-dependent manner. These results not only uncover a novel regulatory mechanism of m^{6}A reader proteins in retinal degeneration but also provide a promising therapeutic target for the development of interventions for IRDs.

DATA AVAILABILITY

The datasets produced and/or analyzed in the current study are available from the corresponding author upon reasonable request. The raw scRNA-seq data generated in this study are available from the NCBI database (BioProjectID PRJNA1224789), China National Center for Bioinformation database of Genome Sequence Archive (GSA) (CRA037343), and Science Data Bank database (https://doi.org/10.57760/sciencedb.j00139.00167).

SUPPLEMENTARY DATA

Supplementary data to this article can be found online

COMPETING INTERESTS

The authors declare that they have no competing interests.

AUTHORS' CONTRIBUTIONS

X.J.Z.: Conceptualization, Methodology, Writing - Review & Editing, Project administration. X.Y.J. and W.J.L.: Investigation, Validation. Y.D.F. and G.L.: Validation. S.Y.: Validation. K.X.S.: Validation. J.Y.C.: Investigation. B.L.: Conceptualization, Methodology, Writing - Review & Editing. Y.M.Y.: Investigation, Methodology, Validation, Writing - Original draft. All authors read and approved the final version of the manuscript.

REFERENCES

Ajmal M, Khan MI, Neveling K, et al. 2014. A missense mutation in the splicing factor gene *DHX38* is associated with early-onset retinitis pigmentosa with macular coloboma. *Journal of Medical Genetics*, **51**(7): 444–448.

Banerjee P, Kleyn PW, Knowles JA, et al. 1998. *TULP1* mutation in two extended dominican kindreds with autosomal recessive retinitis pigmentosa. *Nature Genetics*, **18**(2): 177–179.

Barbieri I, Tzelepis K, Pandolfini L, et al. 2017. Promoter-bound METTL3 maintains myeloid leukaemia by m^{6}A-dependent translation control. *Nature*, **552**(7683): 126–131.

Bawankar P, Lence T, Paolantoni C, et al. 2021. Hakai is required for stabilization of core components of the m^{6}A mRNA methylation machinery. *Nature Communications*, **12**(1): 3778.

Butler A, Hoffman P, Smibert P, et al. 2018. Integrating single-cell transcriptomic data across different conditions, technologies, and species. *Nature Biotechnology*, **36**(5): 411–420.

Chen SJ, Zhu GH, Yang Y, et al. 2021. Single-cell analysis reveals transcriptomic remodellings in distinct cell types that contribute to human prostate cancer progression. *Nature Cell Biology*, **23**(1): 87–98.

Eldred KC, Avelis C, Johnston Jr RJ, et al. 2020. Modeling binary and graded cone cell fate patterning in the mouse retina. *PLoS Computational Biology*, **16**(3): e1007691.

Grossman GH, Pauer GJT, Narendra U, et al. 2009. Early synaptic defects in *tulp1*$^{-/-}$ mice. *Investigative Ophthalmology & Visual Science*, **50**(7): 3074–3083.

Gu SM, Lennon A, Li Y, et al. 1998. Tubby-like protein-1 mutations in autosomal recessive retinitis pigmentosa. *The Lancet*, **351**(9109): 1103–1104.

Hagstrom SA, Adamian M, Scimeca M, et al. 2001. A role for the Tubby-like protein 1 in rhodopsin transport. *Investigative Ophthalmology & Visual Science*, **42**(9): 1955–1962.

Hagstrom SA, Duyao M, North MA, et al. 1999. Retinal degeneration in *tulp1*$^{-/-}$ mice: vesicular accumulation in the interphotoreceptor matrix. *Investigative Ophthalmology & Visual Science*, **40**(12): 2795–2802.

Hagstrom SA, North MA, Nishina PM, et al. 1998. Recessive mutations in the gene encoding the tubby-like protein TULP1 in patients with retinitis pigmentosa. *Nature Genetics*, **18**(2): 174–176.

Hassan IU, Rehman HM, Liu ZR, et al. 2023. Genome-wide identification and spatiotemporal expression profiling of zinc finger SWIM domain-containing protein family genes. *Zoological Research*, **44**(3): 663–674.

Huang HL, Weng HY, Sun WJ, et al. 2018. Recognition of RNA *N*^{6}-methyladenosine by IGF2BP proteins enhances mRNA stability and translation. *Nature Cell Biology*, **20**(3): 285–295.

Jia DN, Gao P, Lv YX, et al. 2022. Tulp1 deficiency causes early-onset retinal degeneration through affecting ciliogenesis and activating ferroptosis in zebrafish. *Cell Death & Disease*, **13**(11): 962.

Jia GF, Fu Y, Zhao X, et al. 2011. *N*6-methyladenosine in nuclear RNA is a major substrate of the obesity-associated FTO. *Nature Chemical Biology*, **7**(12): 885–887.

Knowles JA, Shugart Y, Banerjee P, et al. 1994. Identification of a locus, distinct from RDS-peripherin, for autosomal recessive retinitis pigmentosa on chromosome 6p. *Human Molecular Genetics*, **3**(8): 1401–1403.

Latif Z, Chakchouk I, Schrauwen I, et al. 2018. Confirmation of the role of *DHX38* in the etiology of early-onset retinitis pigmentosa. *Investigative Ophthalmology & Visual Science*, **59**(11): 4552–4557.

Li JS, Yang XX, Qi ZP, et al. 2019. The role of mRNA m^{6}A methylation in the nervous system. *Cell & Bioscience*, **9**: 66.

Liu JZ, Yue YN, Han DL, et al. 2014. A METTL3–METTL14 complex mediates mammalian nuclear RNA *N*^{6}-adenosine methylation. *Nature Chemical Biology*, **10**(2): 93–95.

Liu SP, Li GH, Li QJ, et al. 2020a. The roles and mechanisms of YTH domain-containing proteins in cancer development and progression. *American Journal of Cancer Research*, **10**(4): 1068–1084.

Liu T, Wei QL, Jin J, et al. 2020b. The m^{6}A reader YTHDF1 promotes ovarian cancer progression via augmenting EIF3C translation. *Nucleic Acids Research*, **48**(7): 3816–3831.

Livneh I, Moshitch-Moshkovitz S, Amariglio N, et al. 2020. The m^{6}A epitranscriptome: transcriptome plasticity in brain development and function. *Nature Reviews Neuroscience*, **21**(1): 36–51.

Ma LF, Chen TX, Zhang X, et al. 2021. The m^{6}A reader YTHDC2 inhibits lung adenocarcinoma tumorigenesis by suppressing SLC7A11-dependent antioxidant function. *Redox Biology*, **38**: 101801.

Mataftsi A, Schorderet DF, Chachoua L, et al. 2007. Novel TULP1 mutation causing leber congenital amaurosis or early onset retinal degeneration. *Investigative Ophthalmology & Visual Science*, **48**(11): 5160–5167.

Menon M, Mohammadi S, Davila-Velderrain J, et al. 2019. Single-cell transcriptomic atlas of the human retina identifies cell types associated with age-related macular degeneration. *Nature Communications*, **10**(1): 4902.

Meyer KD, Patil DP, Zhou J, et al. 2015. 5′ UTR m^{6}A promotes cap-independent translation. *Cell*, **163**(4): 999–1010.

Nadal-Nicolás FM, Galindo-Romero C, Lucas-Ruiz F, et al. 2023. Pan-retinal ganglion cell markers in mice, rats, and rhesus macaques. *Zoological Research*, **44**(1): 226–248.

Nassisi M, Smirnov VM, Solis Hernandez C, et al. 2021. *CNGB1*‐related rod‐cone dystrophy: a mutation review and update. *Human Mutation*, **42**(6): 641–666.

Niu FG, Che PF, Yang ZX, et al. 2022a. M^{6}A regulation of cortical and retinal neurogenesis is mediated by the redundant M^{6}A readers ythdfs. *iScience*, **25**(9): 104908.

Niu FG, Han P, Zhang J, et al. 2022b. The m^{6}A reader YTHDF2 is a negative regulator for dendrite development and maintenance of retinal ganglion cells. *eLife*, **11**: e75827.

Obuća M, Cvačková Z, Kubovčiak J, et al. 2022. Retinitis pigmentosa-linked mutation in DHX38 modulates its splicing activity. *PLoS One*, **17**(4): e0265742.

Petersen-Jones SM, Occelli LM, Winkler PA, et al. 2018. Patients and animal models of CNGβ1-deficient retinitis pigmentosa support gene augmentation approach. *The Journal of Clinical Investigation*, **128**(1): 190–206.

Ping XL, Sun BF, Wang L, et al. 2014. Mammalian WTAP is a regulatory

subunit of the RNA N6-methyladenosine methyltransferase. *Cell Research*, **24**(2): 177–189.

Shi HH, Chai PW, Jia RB, et al. 2020. Novel insight into the regulatory roles of diverse RNA modifications: re-defining the bridge between transcription and translation. *Molecular Cancer*, **19**(1): 78.

Shi HL, Zhang XL, Weng YL, et al. 2018. m^{6}A facilitates hippocampus-dependent learning and memory through YTHDF1. *Nature*, **563**(7730): 249–253.

Sun RX, Zhu HJ, Zhang YR, et al. 2023. ALKBH5 causes retinal pigment epithelium anomalies and choroidal neovascularization in age-related macular degeneration via the AKT/mTOR pathway. *Cell Reports*, **42**(7): 112779.

Wang X, Lu ZK, Gomez A, et al. 2014. *N*^{6}-methyladenosine-dependent regulation of messenger RNA stability. *Nature*, **505**(7481): 117–120.

Wang X, Zhao BS, Roundtree IA, et al. 2015. *N*^{6}-methyladenosine modulates messenger RNA translation efficiency. *Cell*, **161**(6): 1388–1399.

Wang YH, Zhang LF, Ren H, et al. 2021. Role of Hakai in m^{6}A modification pathway in *Drosophila*. *Nature Communications*, **12**(1): 2159.

Winkler R, Gillis E, Lasman L, et al. 2019. m^{6}A modification controls the innate immune response to infection by targeting type I interferons. *Nature Immunology*, **20**(2): 173–182.

Wu R, Li A, Sun BF, et al. 2019. A novel m^{6}A reader Prrc2a controls oligodendroglial specification and myelination. *Cell Research*, **29**(1): 23–41.

Xia M, Jiao L, Wang XH, et al. 2023. Single-cell RNA sequencing reveals a unique pericyte type associated with capillary dysfunction. *Theranostics*, **13**(8): 2515–2530.

Xin YL, He QH, Liang HL, et al. 2022. m^{6}A epitranscriptomic modification regulates neural progenitor-to-glial cell transition in the retina. *eLife*, **11**: e79994.

Yang XM, Lin YX, Chen TQ, et al. 2023. YTHDF1 enhances chondrogenic differentiation by activating the wnt/β-catenin signaling pathway. *Stem Cells and Development*, **32**(5-6): 115–130.

Yang YM, Cai JS, Yang X, et al. 2022a. Dysregulated m6A modification promotes lipogenesis and development of non-alcoholic fatty liver disease and hepatocellular carcinoma. *Molecular Therapy*, **30**(6): 2342–2353.

Yang YM, Jiang XY, Chen JY, et al. 2024. The m^{6}A reader YTHDC2 maintains visual function and retinal photoreceptor survival through modulating translation of PPEF2 and PDE6B. *Journal of Genetics and Genomics*, **51**(2): 208–221.

Yang YM, Li X, Wang JP, et al. 2021. A missense mutation in *Pitx2* leads to early-onset glaucoma via NRF2-YAP1 axis. *Cell Death & Disease*, **12**(11): 1017.

Yang YM, Liu WJ, Sun KX, et al. 2019. *Tmem30a* deficiency leads to retinal rod bipolar cell degeneration. *Journal of Neurochemistry*, **148**(3): 400–412.

Yang YM, Shuai P, Li X, et al. 2022b. Mettl14-mediated m6A modification is essential for visual function and retinal photoreceptor survival. *BMC Biology*, **20**(1): 140.

Yu J, She YC, Yang LX, et al. 2021. The m^{6}A readers YTHDF1 and YTHDF2 synergistically control cerebellar parallel fiber growth by regulating local translation of the key Wnt5a signaling components in axons. *Advanced Science*, **8**(22): 2101329.

Yue YN, Liu J, Cui XL, et al. 2018. VIRMA mediates preferential m6A mRNA methylation in 3′ UTR and near stop codon and associates with alternative polyadenylation. *Cell Discovery*, **4**(1): 10.

Zheng GQ, Dahl JA, Niu YM, et al. 2013. ALKBH5 is a mammalian RNA demethylase that impacts RNA metabolism and mouse fertility. *Molecular Cell*, **49**(1): 18–29.

Zhuang MR, Geng XQ, Han P, et al. 2023. YTHDF2 in dentate gyrus is the m^{6}A reader mediating m^{6}A modification in hippocampus-dependent learning and memory. *Molecular Psychiatry*, **28**(4): 1679–1691.

Zhuang MR, Li XB, Zhu JD, et al. 2019. The m^{6}A reader YTHDF1 regulates axon guidance through translational control of Robo3.1 expression. *Nucleic Acids Research*, **47**(9): 4765–4777.